NAVAL POSTGRADUATE SCHOOL

MONTEREY, CALIFORNIA

THESIS

PHOTONIC COMPRESSED SENSING NYQUIST FOLDING RECEIVER

by

Richard N. Shmel

September 2017

Thesis Advisor:	Phillip E. Pace
Second Reader:	Roberto Cristi

THIS PAGE INTENTIONALLY LEFT BLANK

REPORT DOCUMENTATION PAGE

Form Approved OMB No. 0704–0188

1. AGENCY USE ONLY *(Leave Blank)*	2. REPORT DATE	3. REPORT TYPE AND DATES COVERED
	September 2017	Master's Thesis 09-25-2016 to 09-15-2017

4. TITLE AND SUBTITLE

PHOTONIC COMPRESSED SENSING NYQUIST FOLDING RECEIVER

5. FUNDING NUMBERS

6. AUTHOR(S)

Richard N. Shmel

7. PERFORMING ORGANIZATION NAME(S) AND ADDRESS(ES)

Naval Postgraduate School
Monterey, CA 93943

8. PERFORMING ORGANIZATION REPORT NUMBER

9. SPONSORING / MONITORING AGENCY NAME(S) AND ADDRESS(ES)

L3 Mission Integration
10001 Jack Finney Blvd., Greenville, TX 75402

10. SPONSORING / MONITORING AGENCY REPORT NUMBER

11. SUPPLEMENTARY NOTES

The views expressed in this document are those of the author and do not reflect the official policy or position of the Department of Defense or the U.S. Government. IRB Protocol Number: N/A.

12a. DISTRIBUTION / AVAILABILITY STATEMENT

Approved for public release. Distribution is unlimited.

12b. DISTRIBUTION CODE

13. ABSTRACT *(maximum 200 words)*

The use of integrated optical components and how they can be used to implement a compressed sensing microwave photonic receiver are investigated in this thesis. The scope of this research covers the design, simulation, and hardware build of a photonic compressed sensing Nyquist folding receiver that is able to directly undersample wideband RF signals and detect the original Nyquist zone and frequency information. This is achieved by generating a frequency modulated optical impulse train for directly undersampling the RF environment at the antenna. The impulse train undersamples the signals using an optical modulator configuration at 1550 nm and collects the detected samples in a low pass interpolation filter. Two independent photonic receiver architectures are designed and analyzed over the course of this research. Both receiver designs are simulated in the OPTSIM photonic design suite and are able to successfully extract the undersampled signals. The first receiver design proved more effective at representing the signal environment and was constructed using electro-optical hardware. Using off-the-shelf components in a proof-of-concept hardware prototype, we confirmed the simulation results by correctly identifying input test frequencies up to an order of magnitude higher than the sampling frequency.

14. SUBJECT TERMS	15. NUMBER OF PAGES
compressed sensing, undersampling, photonic modulators, NYFR, Nyquist folding, electronic warfare, electronic support, OPTSIM	83
	16. PRICE CODE

17. SECURITY CLASSIFICATION OF REPORT	18. SECURITY CLASSIFICATION OF THIS PAGE	19. SECURITY CLASSIFICATION OF ABSTRACT	20. LIMITATION OF ABSTRACT
Unclassified	Unclassified	Unclassified	UU

NSN 7540-01-280-5500

Standard Form 298 (Rev. 2–89)
Prescribed by ANSI Std. 239–18

THIS PAGE INTENTIONALLY LEFT BLANK

Approved for public release. Distribution is unlimited.

PHOTONIC COMPRESSED SENSING NYQUIST FOLDING RECEIVER

Richard N. Shmel
Second Lieutenant, United States Army
B.S., United States Military Academy, 2016

Submitted in partial fulfillment of the
requirements for the degree of

MASTER OF SCIENCE IN ELECTRICAL ENGINEERING

from the

NAVAL POSTGRADUATE SCHOOL
September 2017

Approved by: Phillip E. Pace
Thesis Advisor

Roberto Cristi
Second Reader

Clark Robertson
Chair, Department of Electrical and Computer Engineering

THIS PAGE INTENTIONALLY LEFT BLANK

ABSTRACT

The use of integrated optical components and how they can be used to implement a compressed sensing microwave photonic receiver are investigated in this thesis. The scope of this research covers the design, simulation, and hardware build of a photonic compressed sensing Nyquist folding receiver that is able to directly undersample wideband RF signals and detect the original Nyquist zone and frequency information. This is achieved by generating a frequency modulated optical impulse train for directly undersampling the RF environment at the antenna. The impulse train undersamples the signals using an optical modulator configuration at 1550 nm and collects the detected samples in a low pass interpolation filter. Two independent photonic receiver architectures are designed and analyzed over the course of this research. Both receiver designs are simulated in the OPTSIM photonic design suite and are able to successfully extract the undersampled signals. The first receiver design proved more effective at representing the signal environment and was constructed using electro-optical hardware. Using off-the-shelf components in a proof-of-concept hardware prototype, we confirmed the simulation results by correctly identifying input test frequencies up to an order of magnitude higher than the sampling frequency.

THIS PAGE INTENTIONALLY LEFT BLANK

Table of Contents

1 Introduction **1**

1.1 Background and Motivation 1

1.2 Principal Contribution 2

1.3 Thesis Organization 3

2 Nyquist Folding Methodology **5**

2.1 Analog-to-Information Receiver 5

2.2 Unfolding the Undersampled Signals 7

3 Receiver Operation and Design **9**

3.1 Integrated Optical Components 9

3.2 Double-Modulator Design Concept 13

3.3 Single-Modulator Design Concept 17

3.4 Design Constraints and Considerations 18

4 Photonic NYFR Computer Simulations **23**

4.1 DM-NYFR Computer Simulation 23

4.2 SM-NYFR Computer Simulation 32

5 Receiver Hardware Prototype Build **37**

5.1 Overall Setup and Equipment Used 37

5.2 MZI Setup and Testing 39

5.3 Pulse Generation Circuit 41

6 Prototype Test and Evaluation **47**

6.1 FM Optical Pulse Testing 47

6.2 Signal Processing Methodology 49

6.3 Single-Tone Test Results 52

7 Conclusion and Future Work **57**
7.1 Conclusion 57
7.2 Future Work 58

Appendix: MATLAB Code **59**

List of References **63**

Initial Distribution List **65**

List of Figures

Figure 2.1 Analog-to-Information Receiver. 6

Figure 3.1 Diagram of Single-Arm MZI. 11

Figure 3.2 Graphic Representation of MZI Function 12

Figure 3.3 DM-NYFR Block Diagram Showing the Overall Architecture of the Receiver 14

Figure 3.4 Example of an Arbitrary Signal Sampled by an Optical Pulse Train 15

Figure 3.5 An Example Linear Chirp Used to Generate a FM Dirac Comb Every Positive-to-Negative Zero Crossing 17

Figure 3.6 SM-NYFR Block Diagram Showing the Overall Architecture of the Receiver 18

Figure 3.7 Maximum Intercept Frequency for Nanosecond Pulse-Widths Illustrating a Low-Cost Prototype Build 21

Figure 3.8 Maximum Intercept Frequency for Picosecond and Sub-Picosecond Pulse-Widths Illustrating a Potential High-Cost Build 21

Figure 4.1 DM-NYFR Computer Simulation Model Showing All Components and Connections 23

Figure 4.2 Electrical Pulse Generation Simulation Outputs 25

Figure 4.3 Optical Pulse Train Output From MZI1 26

Figure 4.4 DM-NYFR Test One 28

Figure 4.5 DM-NYFR Test Two 29

Figure 4.6 Unfolding the Original 2.75 GHz Signal. 30

Figure 4.7 DM-NYFR Test Three Results 31

Figure 4.8 Test Four Results Displaying the Spectrogram of Folded 2.7 GHz and 9.1 GHz Signals 32

Figure 4.9 SM-NYFR Simulation Model with all Blocks Outlined 33
Figure 4.10 5.25 GHz RF Results 34
Figure 4.11 8.1 GHz Target Signal Response 35

Figure 5.1 DM-NYFR Hardware Setup 38
Figure 5.2 JDSU X5 MZI Mounted on a PCB 40
Figure 5.3 Oscilloscope Capture of a Single 30 ns Wide Electrical Pulse Incident on a JDSU X5 MZI 40
Figure 5.4 EPG Circuit Schematic Created in NI Multisim Along with an Example Waveform 42
Figure 5.5 Multisim Simulation Showing the Output of Scope One and Two 43
Figure 5.6 Results of EPG Circuit Testing 44
Figure 5.7 Single Falling Edge with Electrical Pulse 45
Figure 5.8 Electrical Pulses and the Corresponding Optical Pulses 45

Figure 6.1 FM Optical Pulse Train PRI 48
Figure 6.2 Time-Frequency Spectrogram of FM Optical Pulses 49
Figure 6.3 Example NYFR Capture Illustrating Both the Signal and Optical Noise. 50
Figure 6.4 Block Diagram of NYFR Image Processing Steps 50
Figure 6.5 Example NYFR Capture Histogram Illustrating Otsu's Method of Optimal Thresholding 52
Figure 6.6 225 kHz Test with Preset Three 53
Figure 6.7 225 kHz Signal with a Fitted Slope for Unfolding 54
Figure 6.8 525 kHz Test with Preset Four 55
Figure 6.9 Nyquist Zone Overflow at 1.75 ms 56

List of Tables

Table 4.1 Component Labels, Names, and Descriptions From the DM-NYFR Computer Simulation Model 24

Table 4.2 SM-NYFR Component Labels, Names, and Descriptions from the SM-NYFR Computer Simulation Model. 33

Table 5.1 DM-NYFR Prototype Hardware Build Component Descriptions . . 39

Table 6.1 Pulse Train FM Presets 47

THIS PAGE INTENTIONALLY LEFT BLANK

List of Acronyms and Abbreviations

ADC	Analog-to-Digital Converter
CW	Continuous Wave
ELINT	Electronic Intelligence
EW	Electronic Warfare
FM	Frequency Modulated
LNA	Low Noise Amplifier
LPF	Low Pass Filter
MZI	Mach-Zehnder Interferometer
NYFR	Nyquist folding receiver
PRF	Pulse-Repetition Frequency
PRI	Pulse-Repetition Interval
RF	Radio Frequency
SIGINT	Signals Intelligence

THIS PAGE INTENTIONALLY LEFT BLANK

Acknowledgments

Sincere thanks to my advisor, Professor Pace, for his unwavering support and patience while I worked on this thesis. Thanks to my second reader, Professor Cristi, for assisting with the writing process. I would also like to thank the staff and faculty of the NPS ECE department for all the assistance provided. Thank you also to L3's Dr. Susan Wilson, Dr. Jerry Fudge, and Dr. Frank Boyle, who provided an immense amount of support and guidance through the CRADA. Special thanks to P. Balasubramanium at Rohde & Schwarz for helping with the signal generators and test equipment.

THIS PAGE INTENTIONALLY LEFT BLANK

CHAPTER 1:
Introduction

Wideband spectrum analysis of electromagnetic waveforms is constrained by many factors. Traditional receivers are limited by sampling speeds that must meet the Nyquist criterion and components with limited bandwidths, both of which prevent wideband interception of the radio frequency (RF) environment. The design, simulation, and prototyping of a photonic Nyquist folding receiver that alleviates many of the limiting factors that restrict current wideband signal collection are discussed in this thesis.

1.1 Background and Motivation

Electronic intelligence (ELINT) is intelligence gathering using electronic sensors focused on RF signals-of-interest. Target signals vary wildly, ranging from radar, navigation beacons, jammers, radio control links, guidance systems, and identification friend or foe (IFF) systems [1]. Signals intelligence (SIGINT) is related to ELINT but is primarily focused on communication signals. These terms are often used interchangeably in electronic warfare (EW) literature. EW Receivers measure pulsed and low probability of intercept (LPI) signals and determine their carrier frequencies, pulse characteristics, phase or frequency variations, and polarization [1]. The Nyquist folding receiver (NYFR) described in this thesis is able to provide pulse rate, carrier frequency, phase variation, and frequency variation information while utilizing a compressed sensing methodology.

The primary motivation for this thesis is to apply compressed sensing techniques to a new receiver design implemented with wideband integrated optical components. Progress with photonic devices is rapidly surpassing conventional electronic systems. Digital EW receivers are taking advantage of these advances in order to digitize and process wide spectrum bandwidths. Specifically, optical receivers have an advantage in bandwidth, sampling speed, and immunity to electromagnetic interference. Photonic $LiNbO_3$ modulators now have bandwidths on the order of 40 GHz and can efficiently couple RF-antenna signals directly into the optical domain [2]. Mode-locked lasers used for sampling now have tunable femtosecond-wide pulse widths with pulse-repetition frequencies (PRF) on the order of 300 GS/s to allow over sampling of complex modulations [3].

1.2 Principal Contribution

The research objective for this thesis is to determine if integrated photonic components can be used to implement a NYFR compressed sensing receiver configured in the optical domain as well as characterize the functionality, performance, and limitations of these types of photonic receiver architectures. The principal contribution of this thesis is the development of a novel compressed sensing receiver that takes advantage of optical signal processing techniques. Detailed in this thesis is the entire engineering process from the initial architectural designs, through computer simulations, and ending in a hardware prototype of the concept. Additional contributions of the research include developing a robust method of generating frequency modulated optical pulses and analyzing the functional limitations of photonic sampling. Lastly, the construction of a hardware prototype takes the research beyond computer simulations and confirms the physical operation of the receiver design. The research methodology was broken up into three primary research blocks spanning the designs, simulations, and a hardware prototype build.

In the first research block, we focus on developing a feasible compressed sensing architecture in the optical domain. The NYFR receiver relies on frequency swept optical pulses to function as a sampling impulse train. Initially, two separate designs were investigated for implementing a modulated sampling impulse function. The first design examined using two separate optical modulators coupled together with one modulator generating an optical sampling impulse train and the other incepting the target RF signal. Sampling pulses are generated electrically using an electrical pulse generator which is connected to a modulator to convert electrical impulses into optical impulses. The sampling frequency modulated (FM) Dirac function is coupled to a second modulator that incepts the antenna signal onto the optical pulses. This novel sampling method utilizing two modulators is a principal thesis contribution. After sampling the RF environment, the optical waveform is coupled to a photodiode and amplifier for envelope detection and later digitization. A second architecture developed during the research utilizes a single modulator to incept the RF signal which is sampled by an analog-to-digital converter (ADC). The trigger for the ADC is modulated in order to achieve non-uniform sampling.

Next, both designs are simulated in the OPTSIM photonic design suite in order to confirm the functionality of the NYFR compressed sensing receiver. This was a critical step because it allowed the designs to be quickly tested and their limitations confirmed. The

test results using simulated RF signals showed that the designs were successful in unfolding undersampled waveforms in the optical domain, establishing a foundation for future work and confirming the receiver's effectiveness. Test results indicated that the two modulator architecture had superior performance.

After successful undersampling with RF signals above the Nyquist rate, the next block of research focused on a prototype hardware build that could function as a proof-of-concept technology demonstrator. Translating a theoretical model into a functional receiver required designing a novel electrical pulse-generator circuit that outputs a pulse train with a frequency modulated pulse-to-pulse interval. After successfully incepting imitation RF signals from a signal generator, the receiver output was sampled and analyzed using digital signal processing (DSP) spectrogram techniques. The signals were analyzed in a time-frequency representation. Significant effort went into de-noising and edge detecting the signals. Hardware tests confirmed the simulation results by correctly unfolding the undersampled signals and is a significant research contribution. Ultimately, the hardware design proved successful in incepting and extracting RF signals and providing a foundation for future work.

1.3 Thesis Organization

This thesis report is organized as follows. The NYFR architecture and governing equations are described in Chapter 2 along with the technical literature relevant to the thesis research. The two photonic NYFR architectures developed for the thesis and the integrated photonic components used in designing the receivers are detailed in Chapter 3. Simulation models and test results which confirmed the theoretical design functionality are shown in Chapter 4. The physical hardware build is described in Chapter 5, along with individual component testing. Selected results from the hardware prototype digital signal processing steps are highlighted in Chapter 6. Lastly, the thesis research is summarized in Chapter 7 along with potential areas for future work. The MATLAB code used to unfold the NYFR signals and the image processing scripts that were used for Chapter 6 are listed in the Appendix.

THIS PAGE INTENTIONALLY LEFT BLANK

CHAPTER 2:
Nyquist Folding Methodology

The model of the photonic receiver presented in this thesis is a compressed sensing method known as Nyquist folding. The relevant NYFR theory, governing equations, and operation is described in this chapter. In order to effectively sample a signal using only one piece of information, the sampling frequency must be greater than twice the maximum signal bandwidth. This is the Nyquist criterion and is written as

$$f_{sam} > 2B_{sig} \tag{2.1}$$

where f_{sam} is the sampling rate, and B_{sig} is the signal bandwidth. Sampling at a rate lower than f_{sam} is called undersampling and causes aliased signals that are symmetrical around $f_{sam}/2$. The NYFR takes advantage of aliasing in order to fold large bandwidths of the RF spectrum into undersampled narrow bandwidths which are later recovered.

2.1 Analog-to-Information Receiver

The NYFR functional block diagram is shown in Figure 2.1(a) along with an illustration of the signed Nyquist zones in Figure 2.1(b). The NYFR uses a wideband front-end filter to select RF frequencies of interest from the environment. The passband must be selected so that the bandwidth is less than or equal to the NYFR maximum intercept frequency. Signals from the wideband filter are sampled by a FM swept clock which is coupled to a narrow band interpolation low pass filter (LPF). Lastly, a uniform sampling analog-to-digital converter digitizes the signal. Unlike traditional receivers which use a uniform sampling rate, the NYFR uses an undersampling rate many times lower than the bandwidth of interest [4].

Target RF signals are aliased into lower frequency zones which are symmetrical around intervals of the undersampling rate ω_s. These are referred to as Nyquist zones and are diagrammed in Figure 2.1(b). The Nyquist zones are named in an alternating sign convention and are each $\omega_s/2$ rad/s wide. If the sampling rate is uniform, these aliased

signals are indistinguishable from the true center frequency; however, the NYFR samples with a modulated linear chirp slope. The sampling waveform imparts a modulation on the target signal which is dependent on the original Nyquist zone of origin [5].

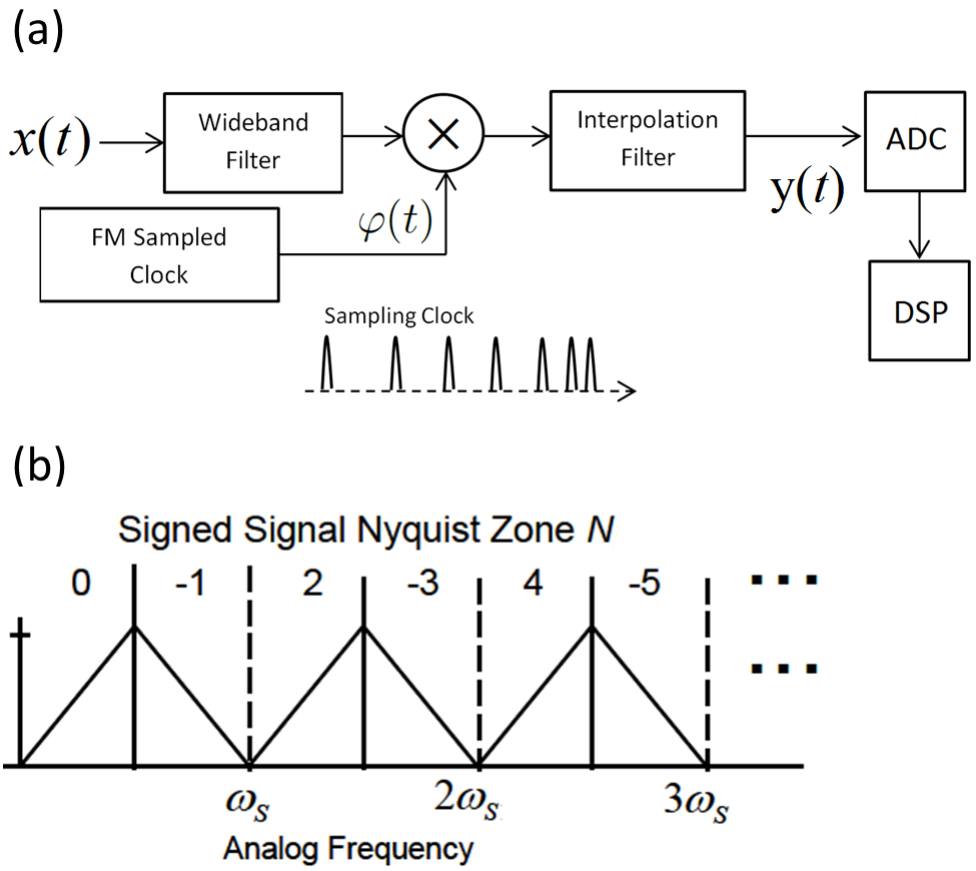

Figure 2.1. Analog-to-information Receiver Showing a) NYFR Operation and b) Signed Nyquist Zones. Adapted from [4].

The FM sampling clock generates a sampling signal centered around an undersampling frequency ω_s with a RF sampling clock modulation $\theta(t)$ as

$$\varphi(t) = \omega_s t + \theta(t) \tag{2.2}$$

and is used to sample the RF spectrum. An example target signal is modeled as

$$x(t) = \cos\left(\omega_c t + \psi(t)\right) \tag{2.3}$$

where ω_c is the center frequency and ψ represents the RF signal information content. Convolving the two signals through the LPF yields the interpolation filter output

$$y(t) = \cos\left(\omega_f t + \beta\psi(t) - M\theta(t)\right) \tag{2.4}$$

where ω_f is the output folded frequency in Nyquist zone $N = 0$, $\beta = sgn(\omega_c - \omega_s k)$ and is the folded spectral orientation, and $M = \beta k$ which is the modulation scale factor [5]. Also, $k = round\left(\omega_c/\omega_s\right)$ and is called the sampling harmonic factor [4], [5]. The induced modulation scale factor M is measurable and $\theta(t)$ is known, so the original signal Nyquist zone can be estimated. Expanding ω_f from (2.4) results in the output folded frequency

$$\omega_f = |\omega_c - \omega_s k| \tag{2.5}$$

which shows the relationship between the sampling modulation and RF center frequency [5].

2.2 Unfolding the Undersampled Signals

In order to extract original frequency information from the aliased signals in Nyquist zone $N = 0$, they must be unfolded and the ambiguities resolved. From (2.4) and (2.5) we see that the modulated RF signal frequency is a function of the original center frequency and the applied chirp modulation. The minimum difference between the signal modulation and clock modulation scaled by the Nyquist zone indicates the signal's original frequency region. The target frequency is extracted from the aliased signal in the $N = 0$ Nyquist zone by first generating an array $Z[i]$ of the modulated signal slope S_m minus the FM clock slope S_c scaled by the signed Nyquist zones $M(i)$. The array is modeled as

$$Z[i] = \left(S_m - M(i)S_c\right)^2 \tag{2.6}$$

where S_c is the slope of the clock modulation, S_m is the slope of the pulse train in time-

frequency analysis, and $M(i)$ is the signed Nyquist zones $N = [0, -1, 2, -3...]$, respectively. The next step is to find the index i of the minimum value of the array so that $i = min\big(Z[i]\big)$. Lastly, the unfolded Nyquist zone is defined by

$$N = sgn\big(M(i)\big)(i - 1) \tag{2.7}$$

where N is the original signed Nyquist zone of the RF signal. Adding the center frequency from Nyquist zone $N = 0$ yields ω_c [6]. This is shown in Section 4.1 for a 2.75-GHz test signal applied to the photonic NYFR simulation.

The NYFR compressed sensing theory and operation was detailed in this chapter by first modeling the NYFR architecture and then describing the governing equations. The analog-to-information process uses clock modulation to impart a slope onto an undersampled signal, which is then used to unfold the aliased waveform. The photonic NYFR designs as well as the integrated optical components used in the architecture are detailed in the next chapter.

CHAPTER 3:
Receiver Operation and Design

The problem presented in this research is the implementation of a photonic NYFR prototype. Correct implementation first requires a detailed design and analysis of required components. Additionally, operating limits and constraints must be taken into account during the design phase. In order to test the feasibility of a photonic compressed sensing receiver, two independent designs are investigated. The first is a purely optical design intended as the primary research contribution of this thesis. The second receiver is an electro-optical solution that functions as an interim design and technology demonstrator for the proposed architecture.

The design phase of the research and the integrated optical components used in the photonic NYFR are described in this chapter. The two receivers are discussed in detail with emphasis on design choices and operating methodology. The constraints of optical sampling components along with each receiver's operating limitations are investigated in the last section.

3.1 Integrated Optical Components

The optical components used to design the NYFR are described in this section. Both design solutions integrate laser sources, optical modulators, and optical detectors in order to undersample and modulate a signal waveform. The specific component types and their operations are expanded upon in subsections.

3.1.1 Semiconductor Laser Source

A continuous wave (CW) semiconductor laser is used as the optical emitter for the NYFR. The specific design is a buried heterostructure laser consisting of a gallium arsenide (GaAs) bandgap junction embedded in an AlGaAs substrate. A wavelength of 1550 nm was used to limit attenuation over the connecting single mode fiber optic cable. The laser operates by applying current above a threshold value I_t, increasing the probability of carrier recombination in the GaAs bandgap and resulting in stimulated emission. The emitted

optical power is written as

$$P_e = \frac{(I - I_t)\eta_i}{e} h\nu \tag{3.1}$$

where I is the applied electric current, h is Planck's constant, ν is the frequency, e is elementary charge, and η_i is the probability of carrier recombination in the gap region [7]. In cases where the laser is modulated directly through the supply current, the applied electric current has both AC and DC components [7]

$$I = I_0 + i_0 e^{i\omega_m t} \tag{3.2}$$

where ω_m is the modulation frequency and I_0 and i_0 are constant DC and AC current magnitudes.

3.1.2 Optical Modulators

Both receiver designs used one or more electro-optic modulators to modulate a CW laser source. Mach-Zehnder Interferometers (MZIs) are used to facilitate amplitude modulation through splitting and recombination of in-phase and out-of-phase beams. The photonic NYFR designs used single-arm MZIs composed of a metallic-infused lithium niobate waveguide channel which splits into two branches at a Y-junction. The upper branch is bracketed by electrodes which apply a voltage potential to the upper waveguide. Voltage applied to the electrodes creates an electromagnetic field through the niobate structure. This alters the β propagation constant on the branch and changes the traveling wave's phase. A second Y-junction recombines the two branches. Depending on the phase difference $\Delta\phi$, we see that the two waves undergo either constructive or destructive interference which modulates the output optical intensity [8]. This is illustrated in Figures 3.1(a) and 3.1(b) for an applied electrode voltage V_a.

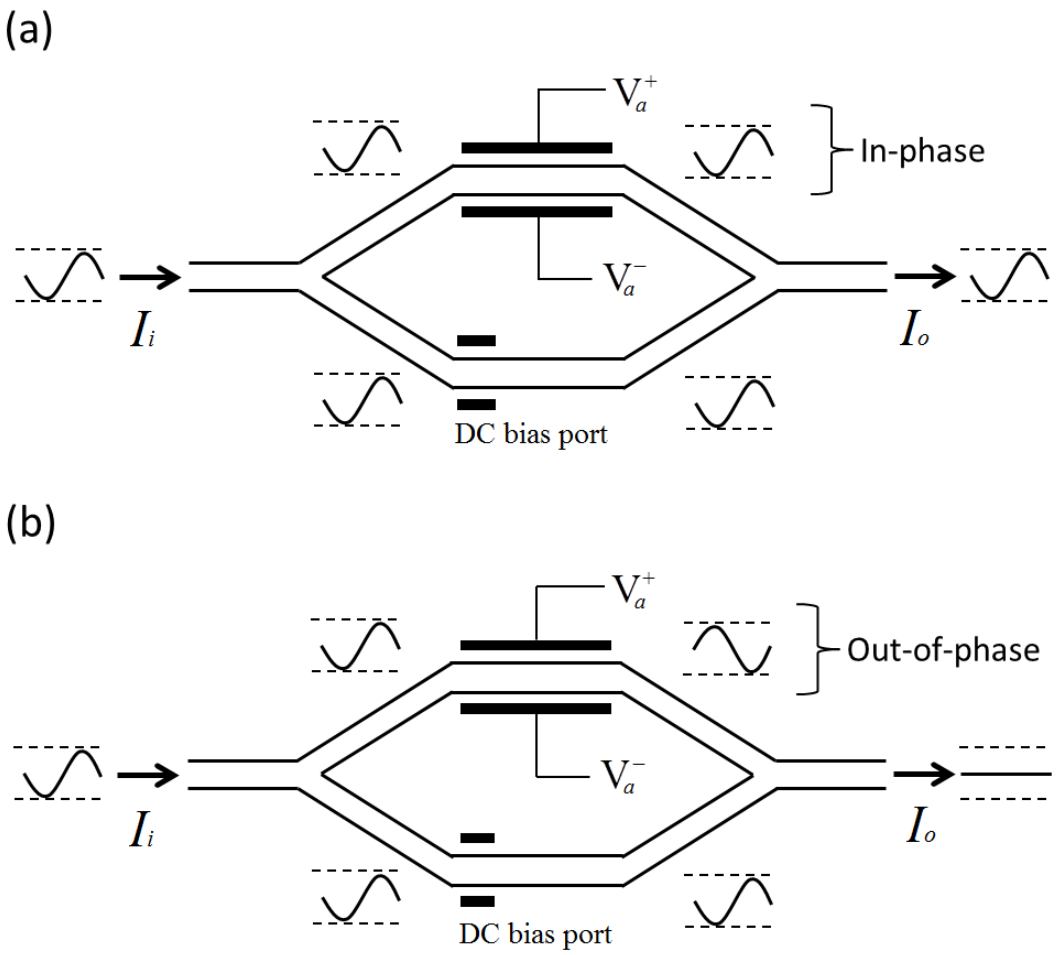

Figure 3.1. Diagram of Single-Arm MZI Showing a) In-Phase Constructive Interference and b) Out-of-Phase Destructive Interference. Adapted from [8].

The output optical intensity I_o of an MZI is a function of the $\Delta\phi$ path length phase difference and is

$$I_o = \frac{I_i}{2}\left[1 + \cos\left(\Delta\phi\right)\right] \tag{3.3}$$

where I_i is the incident optical intensity. The phase difference between the recombining waveforms from each MZI branch is

$$\Delta\phi = \left(\pi \frac{V_a}{V_\pi} + \varphi_o\right) \tag{3.4}$$

where V_π is the switching/threshold voltage, V_a is the applied electrode voltage, and φ_o is an initial phase offset that is built into the device or created with a DC voltage known as a DC bias [9]. When there is a phase difference of $\Delta\phi = \pi$, the output has its lowest value, while a phase difference of zero results in the highest output value. Combining (3.3) and (3.4), we obtain the expanded MZI output intensity

$$I_o = \frac{I_i}{2}\left[1 + \cos\left(\pi \frac{V_a}{V_\pi} + \varphi_o\right)\right]. \tag{3.5}$$

The modulator input/output intensity relationship, or transfer function, is represented graphically in Figure 3.2.

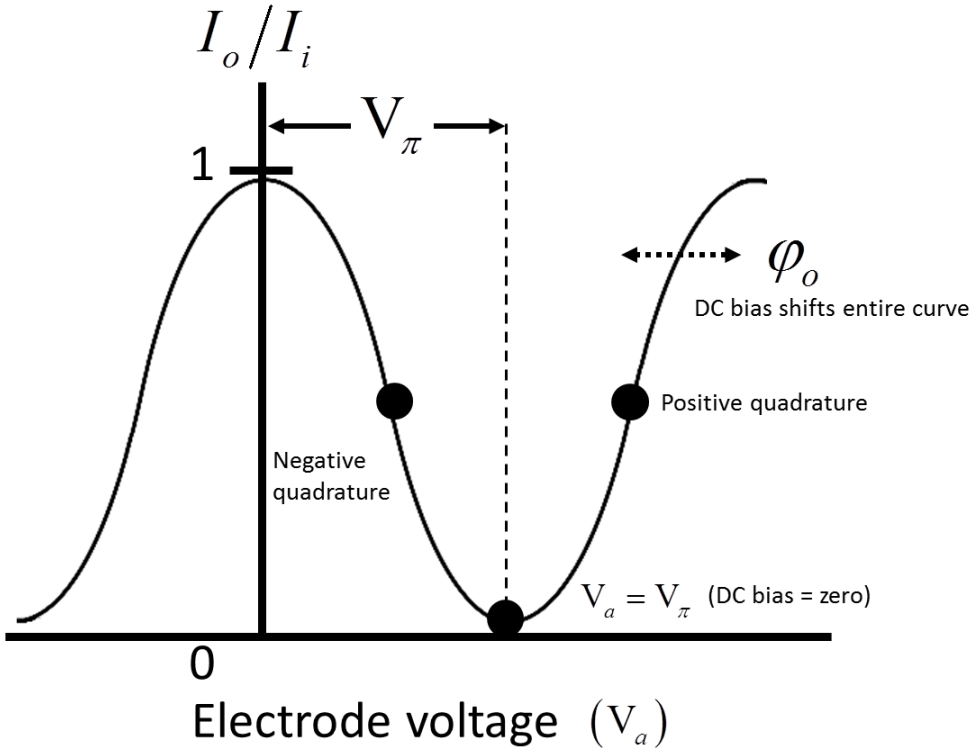

Figure 3.2. Graphic Representation of MZI Function with Both the Quadrature and DC Bias Marked

For a modulator with equal guided-wave path lengths, the application of a DC bias translates the curve left and right. The use of an attenuator or amplifier at the antenna increases or decreases the value of V_π, respectively. This shows the output intensity as a function of the electrode voltage and illustrates the V_π switching voltage. The quadrature point is created by an initial phase constant of $\varphi_o = \pi$ manufactured into the MZI so that any voltage applied shifts the output in the most linear region of operation [10]. This configuration is ideal for coupling an AC small signal onto an optical carrier. The effect of a DC bias is shown as well, where a DC voltage is used to shift the curve such that the initial $V_a = 0$ point is perfectly destructive interference and $V = V_\pi$ is the peak intensity point. This configuration is used for optical pulse generation.

3.1.3 Optical Detectors

The photonic NYFR designs use PIN photodiode detectors to convert optical signals into electrical signals. These detectors consist of p-type and n-type doped silicon separated by an intrinsic region of high resistivity material. Absorption of photons in the silicon material causes electrons to drift and creates current [11]. The NYFR photodiodes are matched to the 1550-nm wavelength of the CW laser. The two most important factors for PIN diodes are gain and frequency response. The NYFR photodiodes have an internal low noise amplifier (LNA) with a 10 dB gain and a frequency response bandwidth of 20 GHz. This response is primarily limited by the transit time of charge carriers separating from the substrate and moving to opposite ends of the depletion region. An internal shunting effect is also present and is calculated as [11]

$$\omega_p = \frac{1}{R_i C_i} \tag{3.6}$$

where ω_p is the photodiode cutoff frequency in rad/s and R_i and C_i are the internal resistance and capacitance of the diode, respectively.

3.2 Double-Modulator Design Concept

The double-modulator NYFR (DM-NYFR) architecture is an implementation of a photonic compressed sensing receiver. It is designed around two MZI modulators. The first

functions as a sampling impulse train generator while the second incepts the RF bandwidth. In the photonic NYFR architecture, the CW laser functions as a carrier for the signal and is analogous to electric current on a wire.

3.2.1 DM-NYFR Operation and Block Diagram

The overall block diagram of the DM-NYFR is shown in Figure 3.3. The front end of the architecture is a fiber-coupled CW laser at 1550 nm. This is connected to the first MZI which converts the CW laser into a sampling pulse train with a linearly swept pulse repetition frequency (PRF). An electrical signal $P(t)$ is connected to the single-arm electrodes of MZI1 and drives the modulation scheme by linearly sweeping a short electrical impulse train. The output optical pulse intensity, represented as I_o, is a function of the frequency and amplitude of the electric signal as well as the MZI transmission (3.5). The front end optical pulse generation is discussed in detail in Section 3.2.2.

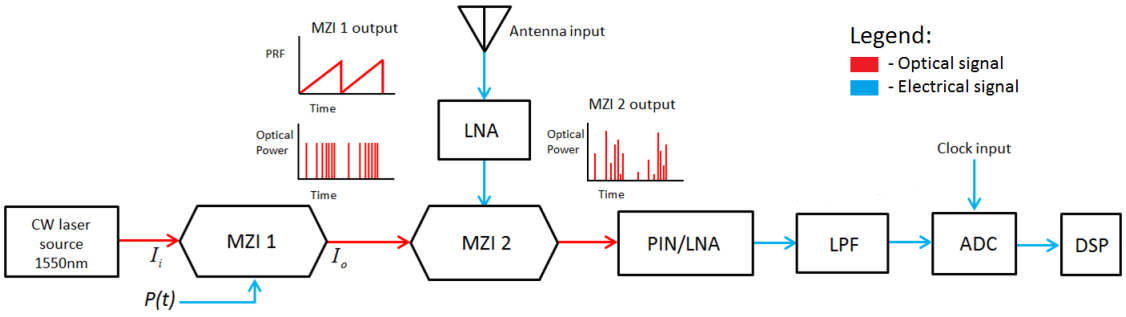

Figure 3.3. DM-NYFR Block Diagram Showing the Overall Architecture of the Receiver

The FM pulse train functions as a sampling signal. When coupled into the second MZI with the RF-signal input, the short-time duration pulses emulate the sampling electrical signal from (2.2). As the FM optical pulse train is passed into MZI2, RF signals from the environment are amplified from an antenna and used to drive MZI2's electrode inputs. The amplitude of the input optical pulses from MZI1 are modulated with the amplified antenna signal voltage, encoding the RF signals as an amplitude modulated (AM) envelope on the sampling pulses. This concept is illustrated in Figure 3.4, in which a diagram of an arbitrary sinusoidal signal encoded on a sampling pulse train is shown. This is a good representation of MZI2's optical output.

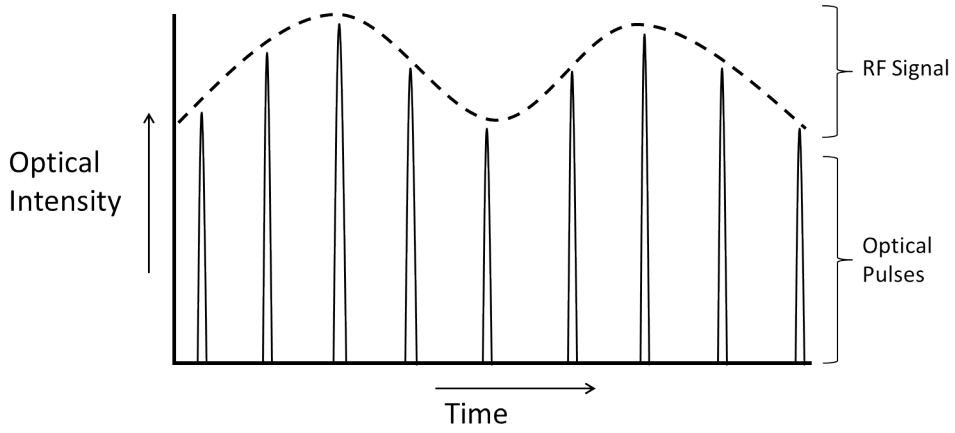

Figure 3.4. Example of an Arbitrary Signal Sampled by an Optical Pulse Train

The output from MZI2 is coupled into a PIN photodiode with an internal LNA in order to convert the optical signal into electrical current. An interpolation low pass filter (LPF) is connected in series to the detector output. The output of the interpolation filter from the photonic NYFR is equivalent to $y(t)$ (2.4). The LPF bandwidth must be greater than or equal to $\omega_s/2$, which is the first Nyquist zone upper frequency shown in Figure 2.1(b). A sampling ADC driven by a clock input at $2\omega_s$ digitizes the information at the required Nyquist rate. Lastly, the ADC passes this information to the digital signal processing (DSP) block where the data is de-noised and unfolded to extract the RF information from the environment.

3.2.2 Optical Pulse Generation

The front end optical pulse generation using MZI1 shown in Figure 3.3 is the most important part of the DM-NYFR architecture. Generating FM optical pulses with small pulse widths enables the NYFR to differentially alias signals to lower Nyquist zones for detection. In the DM-NYFR, optical pulses are generated by applying a pulse signal $P(t)$ to MZI1 so that the coupled CW laser is selectively switched at a linear chirp rate. The electrical pulse signal at the input is modeled as an FM Dirac comb impulse train, comprised of n number of $\delta(t)$ delta functions. This is an approximation, because the Dirac comb impulses have zero pulse width, which is impossible to achieve in actual operation. If the pulse width is much smaller then the RF signal's period, a zero-width impulse train is a

good approximation. As a result, $P(t)$ is represented as a sum of impulses

$$P(t) = V_\pi \sum \delta\big(t - n(t)\big) \tag{3.7}$$

where V_π is the voltage amplitude of the MZI switching voltage and n is the impulse trigger. In order to model the variable PRF of $P(t)$, the delta functions must be triggered from a linear FM sinusoid. In the DM-NYFR architecture, this is modeled as a chirp signal $S_c(t)$, with $n(t)$ set on every positive-to-negative zero crossing such that

$$n(t) = ZCR^{-}\big(S_c(t)\big) \tag{3.8}$$

where ZCR^{-} is the notation for a single-ended zero crossing. For the DM-NYFR, two types of linear chirp signals are used, a sawtooth waveform $S_{c1}(t)$ and a triangular waveform $S_{c2}(t)$. The sawtooth chirp is given by

$$S_{c1}(t) = \sin 2\pi\left(f_c t + \frac{\Delta F}{2t_m}t^2\right) \tag{3.9}$$

where f_c is the center frequency, ΔF is the chirp bandwidth, and t_m is the chirp period. The triangular waveform is defined as

$$S_{c2}(t) = \sin 2\pi\big[S_1(t) + S_2(t)\big] \tag{3.10}$$

with S_1 as the rising chirp sweep and S_2 as the falling chirp sweep. The chirp sweep functions are given by

$$S_1(t) = \left(f_c + \frac{\Delta F}{2}\right)t - \frac{\Delta F}{2t_m}t^2 \tag{3.11}$$

for the positive slope and

$$S_2(t) = \left(f_c - \frac{\Delta F}{2}\right)t + \frac{\Delta F}{2t_m}t^2 \tag{3.12}$$

for the negative slope, where f_c is the center frequency, ΔF is the chirp bandwidth, and t_m is the chirp period [12]. The linear chirp sinusoid (3.9) plotted along with the pulse function (3.8) is detailed in Figure 3.5. Setting the amplitude of the pulse signal to V_π switches the optical modulator at the pulse repetition frequency (PRF) defined by (3.7) and coverts the input CW laser into a sampling impulse train. This illustrates how the front-end pulse generation block works in the DM-NYFR architecture.

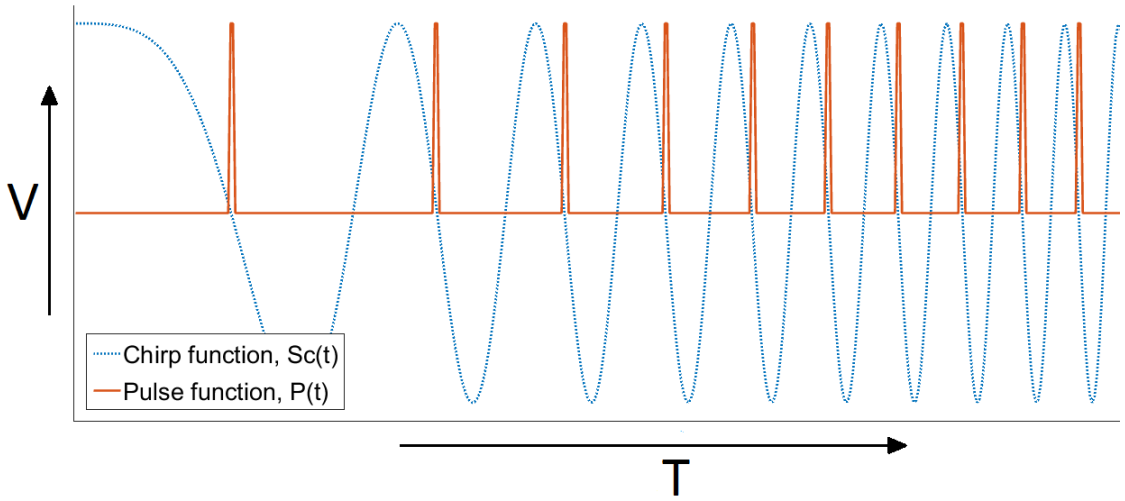

Figure 3.5. An Example Linear Chirp Used to Generate a FM Dirac Comb Every Positive-to-Negative Zero Crossing

3.3 Single-Modulator Design Concept

The single modulator design that serves as a simplified technology demonstrator for the photonic NYFR is described in this section. Conceived as an alternative architecture early in the research process the single-MZI NYFR (SM-NYFR) is an electro-optical hybrid solution that takes advantage of the high bandwidth of photonic components but with the low cost and complexity of electronic sampling devices. The trade off in the electro-optical design is a lower maximum RF-interception frequency than the DM-NYFR solution and higher receiver noise level. The SM-NYFR block diagram is shown in Figure 3.6.

The SM-NYFR uses a CW laser coupled to a single-arm MZI biased at quadrature. The electrodes are attached to an antenna/LNA pair which incepts RF signals from the environment. The high bandwidth of optical components, greater than 40 GHz, ensures that a large RF spectrum is modulated onto the laser. The MZI output is connected to a PIN photodiode, which converts the photonic signal into an electrical signal. The signal is filtered with an interpolating LPF that has a bandwidth greater than the maximum frequency of the first Nyquist zone. An ADC samples the electrical signal driven by a clock pulse $P(t)$ detailed in (3.7). The digital information is processed by a DSP, which unfolds and extracts the RF frequencies from the environment.

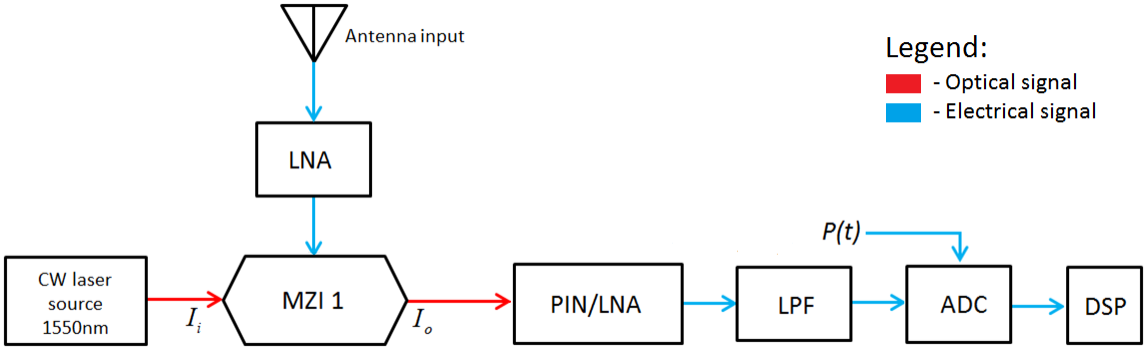

Figure 3.6. SM-NYFR Block Diagram Showing the Overall Architecture of the Receiver

3.4 Design Constraints and Considerations

The photonic NYFR's primary operating boundaries and constraints come from the optical sampling with interferometers. The optical pulse width and ADC resolution determine the maximum frequency that can be modulated onto a laser source. Both pulse width and sampling limitations are examined in detail in this section. The performance of potential hardware builds is also analyzed in order to determine the maximum RF-signal intercept frequencies.

3.4.1 Pulse Width Limitations

The photonic NYFR relies on signal sampling by optical pulses where the instantaneous power of the pulse train is proportional to the sampled waveform. In order to

effectively sample a target RF signal, the pulse width must be smaller than the temporal variation of the modulating signal [13]. The 3 dB bandwidth B_p of an optical pulse is the inverse of the pulse width T_p or $B_p = 1/T_p$. From the Nyquist criterion, the sampling frequency f_s for an arbitrary signal with bandwidth B is $f_s = 2B$, written in terms of pulse width as

$$T_p < \frac{T_s}{2} \tag{3.13}$$

where T_p is the largest allowable pulse width that can effectively sample a signal with a period of T_s. For the photonic NYFR design, this means that optical pulse widths limit the maximum frequency that can be sampled by MZI2, and pulses must be smaller than half the largest RF signal period.

3.4.2 Electro-Optical Sampling Limitations

The optically sampled signal from MZI2 is coupled into a PIN photodiode which converts optical power into an electrical signal. The output voltage must then be quantized by a sampling ADC with finite resolution. Digitizing an analog waveform imparts a sampling error which constrains the photonic NYFR's operating limits. Let the signal applied to the MZI electrodes be

$$V(t) = A\sin(2\pi f_m t) \tag{3.14}$$

where f_m is the maximum signal frequency and A is the signal amplitude [14]. For a sampling pulse width T_p, the error in voltage δV for an arbitrary signal at time t_i in a traveling wave optical device is represented by

$$\delta V = \frac{1}{T_p}\int_{t_i+\frac{T_p}{2}}^{t_i-\frac{T_p}{2}} A\sin(2\pi f_m t)dt - A\sin(2\pi f_m t_i). \tag{3.15}$$

The voltage error is the difference in instantaneous voltage integrated over the width of a sampling pulse. Using a Taylor series expansion to evaluate the integral (3.15) for the

maximum voltage error yields

$$|\delta V|_{max} = \frac{(\pi f_m T_p)^2 A}{6}. \tag{3.16}$$

For a n-bit sampling ADC, the voltage error must be less than half of the level spacing which is

$$|\delta V|_{max} < \frac{2A}{2^n}\left(\frac{1}{2}\right) = \frac{A}{2^n}. \tag{3.17}$$

This results in a T_p pulse width limitation of

$$T_p < \frac{\left(\frac{3}{2^{n-1}}\right)^{1/2}}{\pi f_m} \tag{3.18}$$

where f_m is the maximum target frequency and n is the resolution of the ADC [14].

3.4.3 Implications for Photonic NYFR Design

The electro-optical sampling error associated with the ADC is the dominate limitation for the photonic NYFR architecture. Design implications are shown in Figures 3.7 and 3.8, which are plots of the maximum intercept frequency as a function of pulse width for six and eight bit ADCs, as well as for two separate hardware designs. Figure 3.7 is an illustration of a prototype build using inexpensive off-the-shelf components with pulse widths in the nanosecond range. The upper limit build illustrating picosecond and sub-picosecond pulse widths, which are achievable with either high quality electrical pulse generators or mode locked fiber lasers, is shown in Figure 3.8. There is a clear design trade off between maximum intercept frequency and ADC resolution, with higher resolutions corresponding to lower target RF signals. Additionally, higher frequencies require shorter pulse widths, which increases costs.

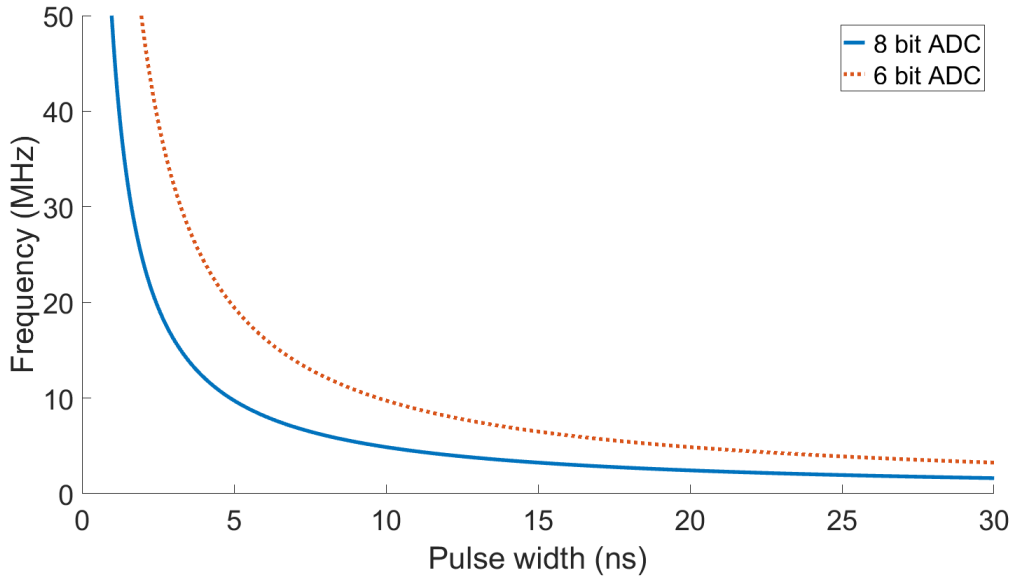

Figure 3.7. Maximum Intercept Frequency for Nanosecond Pulse-Widths Illustrating a Low-Cost Prototype Build

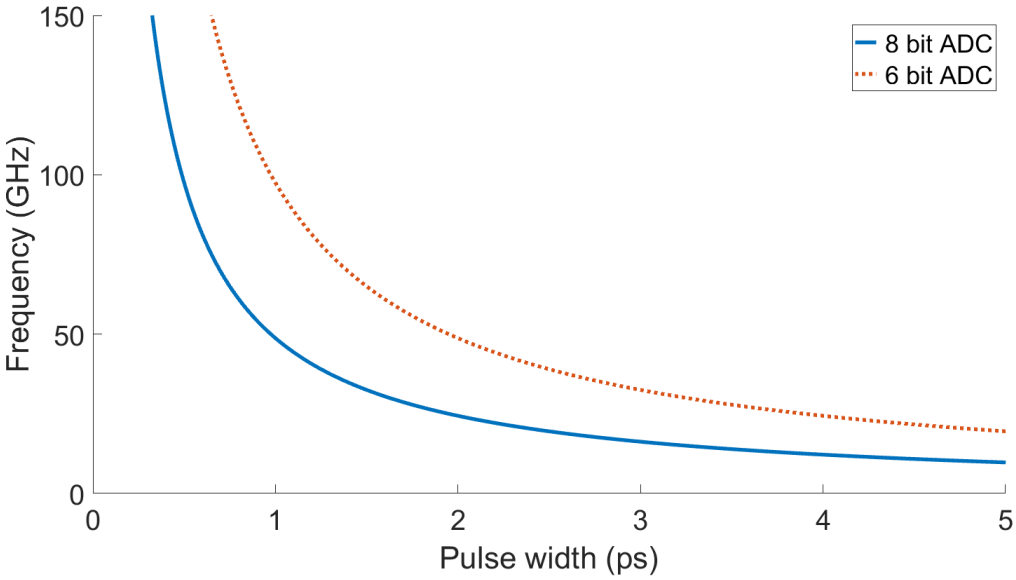

Figure 3.8. Maximum Intercept Frequency for Picosecond and Sub-Picosecond Pulse-Widths Illustrating a Potential High-Cost Build

In summary, both photonic NYFR designs and their operating methodologies were discussed in this chapter. The constraints, limitations, and design trade offs for the photonic

NYFR architecture are examined, and modeling shows that the optical sampling error and the resulting optical pulse width is the primary limiting factor. Additionally, the integrated optical components used in the NYFR are were discussed. The computer simulations and results for both photonic NYFR designs are covered in the next chapter.

CHAPTER 4:
Photonic NYFR Computer Simulations

The computer simulations of the two receiver designs are described in this chapter. Both the DM-NYFR and the SM-NYFR architectures are modeled and simulated in order to test their operation. The final models for both the double and single modulator designs, as well the key test results for each architecture, are detailed in this chapter. Simulation test results were successful in demonstrating correct inception and unfolding of target RF signals.

4.1 DM-NYFR Computer Simulation

The DM-NYFR computer model is shown in Figure 4.1 while Table 4.1, lists the model components and their functions.

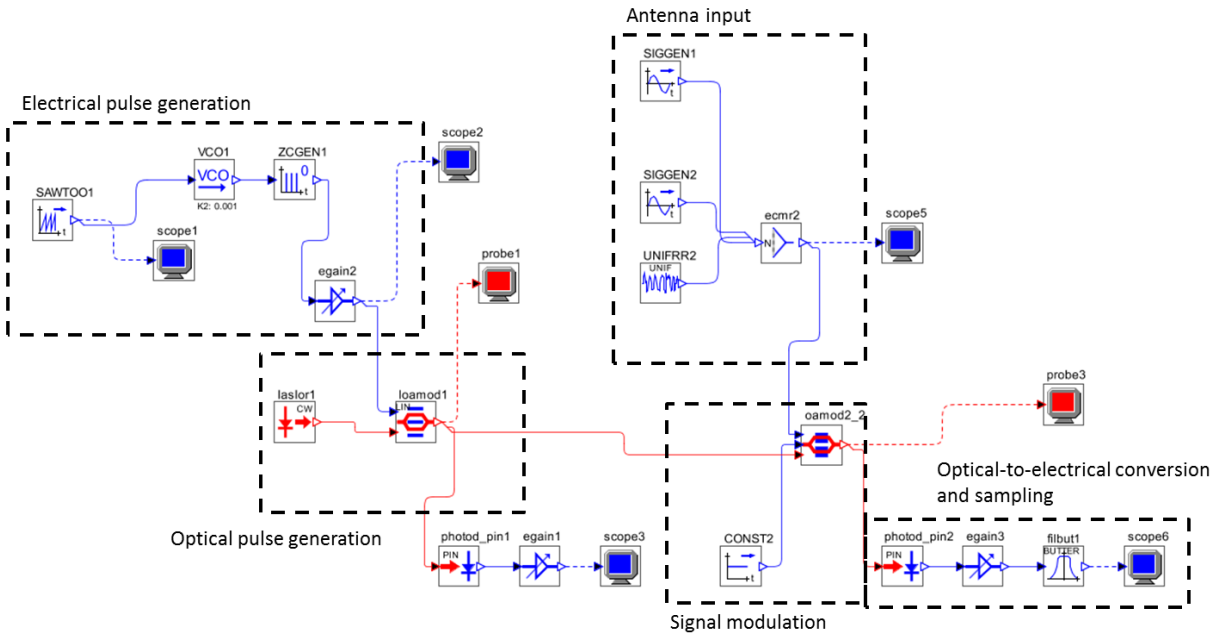

Figure 4.1. DM-NYFR Computer Simulation Model Showing All Components and Connections. Specific Functional Sections are Highlighted and Labeled with Dashed Boxes.

Table 4.1. Component Labels, Names, and Descriptions from the DM-NYFR Computer Simulation Model

Label	**Name**	**Function**
SAWTOO1	Sawtooth wave generator	Generates a electrical sawtooth wave from V_{min} to V_{max} that is fed into the VCO.
VCO1	Voltage controlled oscillator	Generates a linearly chirped sinusoid from the sawtooth input based on voltage sweep.
ZCGEN1	Zero crossing generator	Generates a picosecond wide electrical pulse every positive-to-negative zero crossing.
egain2	Electrical gain	Amplify 1V pulse to V_π (5.5V).
scope1	Electrical scope	Electrical oscilloscope measuring tool.
scope2	Electrical scope	Electrical oscilloscope measuring tool.
laslor1	Laser source	1550nm CW laser source.
loamod1	MZI1	First optical modulator, uses FM electrical pulses to generate FM optical pulses.
probe1	Optical probe	Optical signal measuring tool.
photod_pin1	PIN Photodiode	Converts an optical signal into an electrical signal.
egain1	Electrical gain	Amplify electrical signal from the photodiode.
scope3	Electrical scope	Electrical oscilloscope measuring tool.
SIGGEN1	Signal generator	Generates an electrical target signal for the NYFR
SIGGEN2	Signal generator	Generates an electrical target signal for the NYFR
UNIFRR2	Uniform noise	Adds noise to the signal input
loamod2	MZI2	Modulates the FM pulse train to sample the antenna signal.
probe1	Optical probe	Optical signal measuring tool.
photod_pin2	PIN Photodiode	Converts an optical signal into an electrical signal.
egain3	Electrical gain	Amplify electrical signal from the photodiode.
filbut1	Butterworth LPF	8th order butterworth LPF set to $2f_s$.
scope6	Electrical scope	Electrical oscilloscope measuring tool.

The DM-NYFR design uses two coupled MZIs to both sample and incept a RF signal from the environment. The most important aspect of the design is a front-end optical pulse

generation block that converts a CW laser into a FM optical pulse train. The computer model is broken up into functional sections that each perform a specific task. As shown in Figure 4.1, the sections are electrical pulse generation, optical pulse generation, signal modulation, antenna input, and sampling. The rSoft OPTSIM design suite from Synopsys is used as a photonics modeling environment. This software package enables high fidelity simulation of integrated optical systems, and both receiver designs were successfully simulated and tested. OPTSIM uses a block simulation design environment where components and functions are modeled as discrete units that are linked in a user interface.

4.1.1 Electrical Pulse Generation

The electrical pulse generation block models (3.8) in the rSoft design suite and functions as a proof-of-concept for a hardware build. An electrical signal generator outputs a sawtooth waveform, varying the amplitude from V_{min} to V_{max} over a modulation period t_m. The signal is sent to a voltage controlled oscillator (VCO) that chirps a sinusoid wave from f_{min} to f_{max}. For the VCO operation, V_{min} maps to f_{min} and V_{max} maps to f_{max}. The modulation period matches t_m. The chirped sinusoidal wave from the VCO is sent to a zero crossing pulse generator that outputs a 1.0V electrical pulse with a picosecond-wide pulse width every positive-to-negative transition. In order to modulate the CW laser, the 1.0V pulse train is amplified to the MZI switching voltage V_π. This is shown in Figure 4.2.

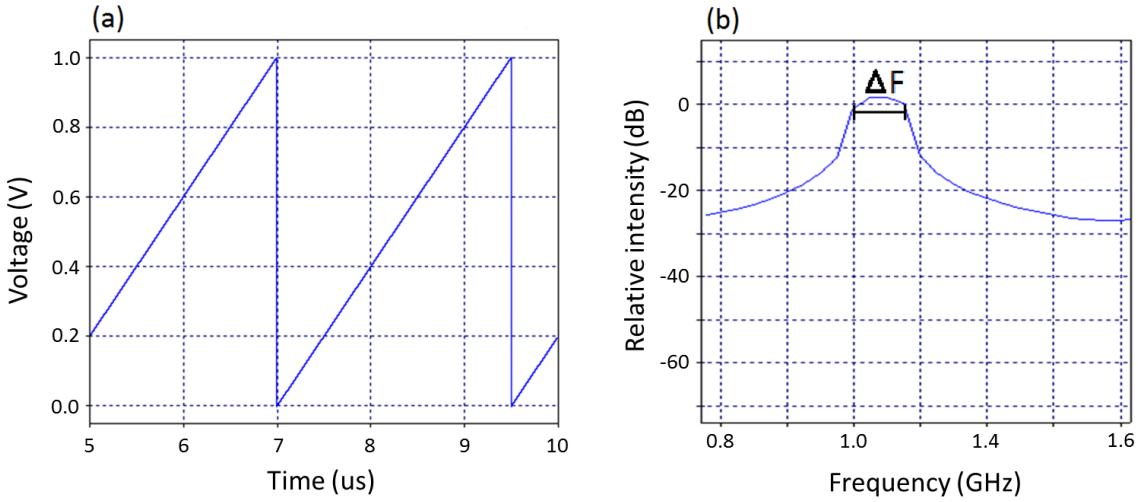

Figure 4.2. Electrical Pulse Generation Simulation Outputs With A) Input Sawtooth Waveform and B) Output Pulse Train Frequency Representation Showing FM Chirp

Figure 4.2(a) is an illustration of the input sawtooth waveform as a time-amplitude representation from scope one. Figure 4.2(b) is an illustration of the output bandwidth of the pulses sampled at scope two. The x-axis is frequency, and the y-axis is relative power in dB. This shows a wide bandwidth ΔF which is the chirp optical pulse train.

4.1.2 Optical Pulse Generation

Electrical pulses are used to drive the first MZI and generate optical pulses as in (3.7). The MZI is simulated as a single-arm cosine squared modulator. The FM optical pulse train is shown in Figure 4.3, which is a MATLAB spectrogram of the data from probe one. Spectrograms use a short time Fourier transform (STFT) window scanned over a signal to make a time-frequency representation of the waveform. The optical pulses are chirped in a sawtooth pattern from the driver signal on the MZI. The input pulses are centered at 1.0 GHz and modulated with $t_m = 5$ μs and $\Delta F = 150$ MHz. The output optical pulses in Figure 4.3 match the MZI inputs, indicating a successful modulation technique.

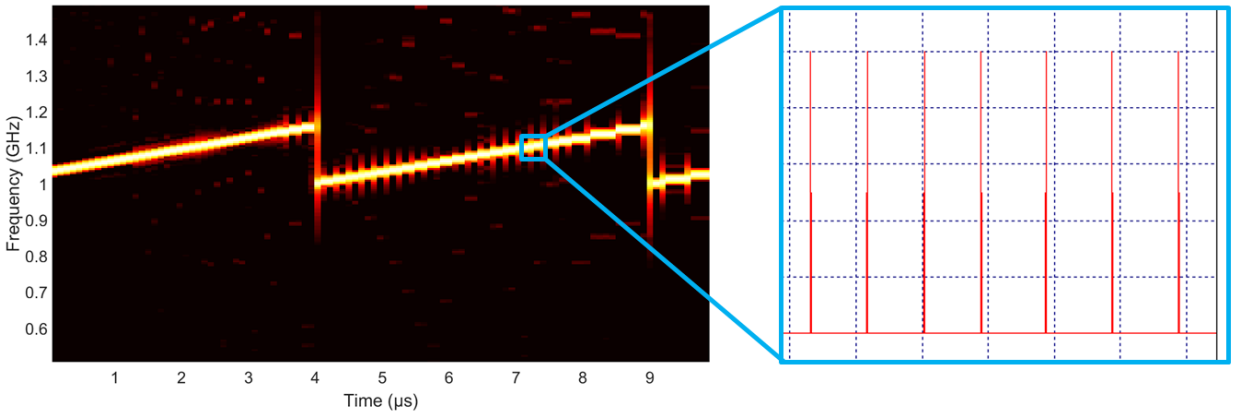

Figure 4.3. Optical Pulse Train Output from MZI1. The Spectrogram Shows a Successful FM Pulse Sweep Taken from Probe One.

4.1.3 Antenna Input and Signal Modulation

The antenna input is comprised of an adjustable number of sinusoidal signal components combined in parallel with a uniform noise generation block. This allows variations in the signal-to-noise ratio (SNR) for testing. The input signals are single frequency tones due to software limitations. The antenna block drives MZI2, and the input optical pulses

sample the RF signals. The resulting signal information is converted from the optical domain into the electrical domain and then filtered and collected in an interpolation LPF. The LPF output is sampled by scope six with sampling rate $2\omega_s$ and piped into MATLAB for signal processing.

4.1.4 DM-NYFR Simulation Results

The simulated DM-NYFR architecture is tested with target signals in order to see if the model can successfully undersample and modulate signals for recovery by the DSP. The simulation is conducted with a sawtooth FM modulation. The modulation period $t_m = 5.0$ μs with $f_{min} = 1$ GHz and $f_{max} = 1.15$ GHz resulting in a ΔF sweep bandwidth of 150 MHz. From Figure 2.1 this gives Nyquist zones every 500 MHz, with zone $N = 0$ from 0 to 500 MHz. The test results show the first two Nyquist zones ($N = 0, -1$) as well as the modulation signal. Scope six, the sampling ADC, has a $2f_s$ sampling rate of 2.0 GHz, and the LPF cutoff frequency is $2f_s$. For all conducted tests, the SNR was 10 dB [15].

Test One: No Modulation

The first test checks the architectures response with no FM sweep applied to the first MZI and the results are shown in Figure 4.4.

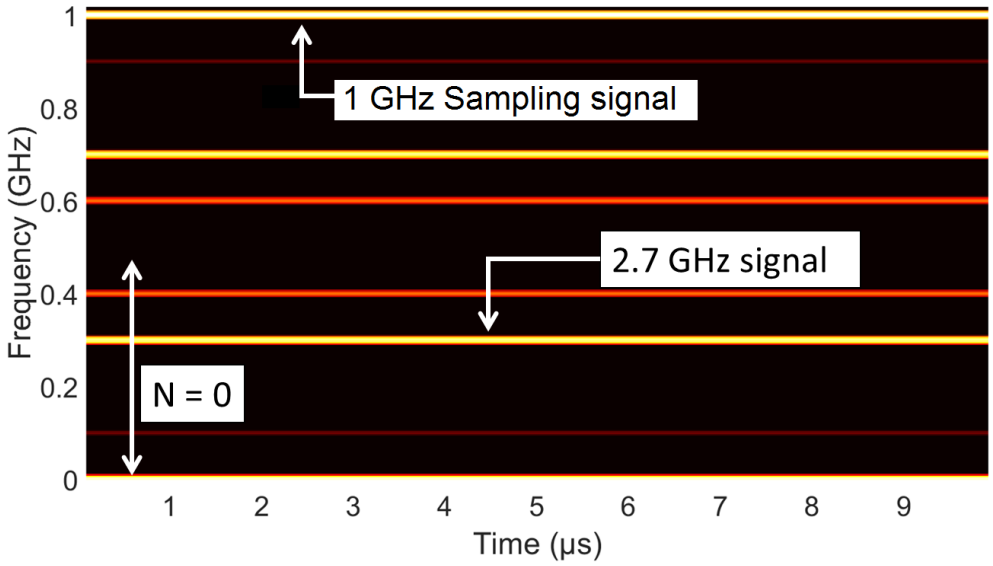

Figure 4.4. DM-NYFR Test One: No Modulation. Disconnected VCO Re-sults in Aliased Signals which Are Unresolvable to Their Original Frequencies.

The VCO was disconnected, so the sampling pulse train had a constant frequency of 1.0 GHz. The applied signal is 2.7 GHz, so the expected results when examining the DSP output are aliased signals centered around 500.0 MHz. The output shown in Figure 4.4 confirms the architecture with no modulation. Aliased signals at 0.3 GHz and 0.7 GHz are seen along with the 1.0 GHz sampling signal. Without modulation the undersampled signals cannot be resolved to their original frequencies.

Test Two: 2.75 GHz Signal

The second test is the architectures response with the FM sweep enabled. The optical pulse train has an FM chirp and successfully undersamples the signal. The target signal is 2.75 GHz, chosen because that is a common aerial search radar frequency. The received signal is shown in Figure 4.5 in the $N = 0$ Nyquist zone with a modulated slope from the MZI1 driver signal. The results are a time-frequency spectrogram computed in MATLAB. Two Nyquist zones, $N = 0, -1$, are shown completely, and are mirror images of each other. Also visible is sampling signal from 1.0 to 1.15 GHz.

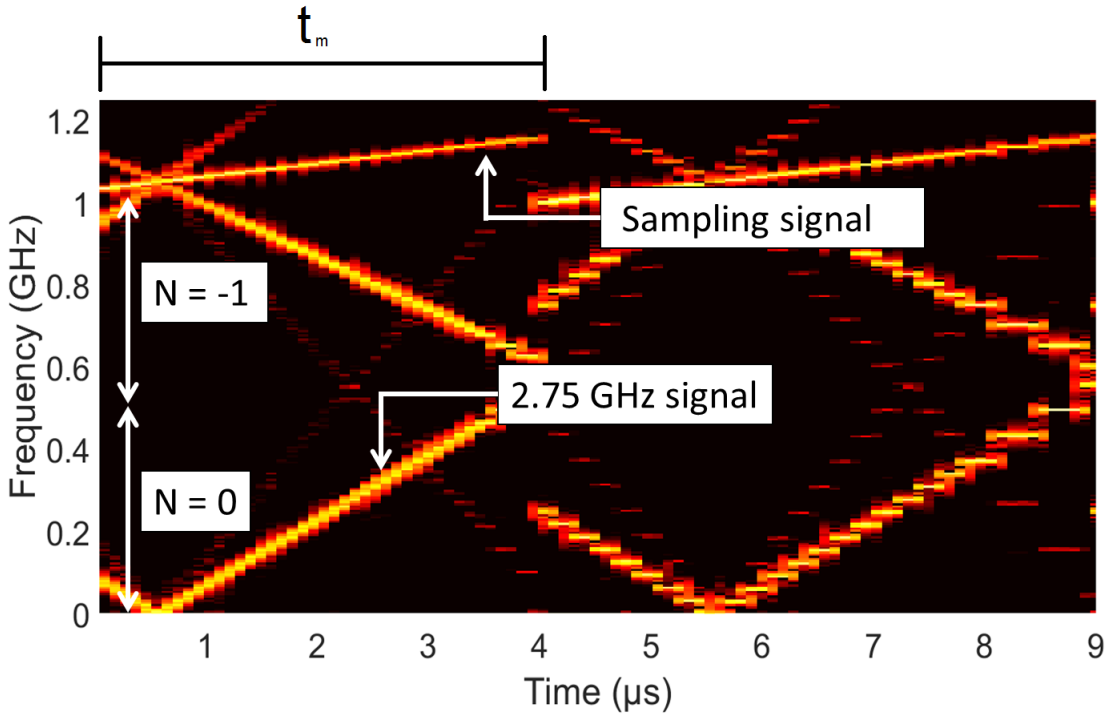

Figure 4.5. DM-NYFR Test Two: 2.75 GHz Signal. Sampling FM Pulses Successfully Modulating a Signal Using NYFR Architecture.

From (2.6) and (2.7), the original frequency can be extracted from the sampling signal and the folded signal. A MATLAB program is used to unfold the signal, and the results are displayed in Figure 4.6. The lowest difference is Nyquist zone $N = -5$, which corresponds to signals between 2.5 and 3.0 GHz. Estimating a center frequency of approximately 0.15 GHz from Figure 4.5 and adding it to the lower frequency bound of the Nyquist zone yeilds the correct original frequency of 2.75 GHz.

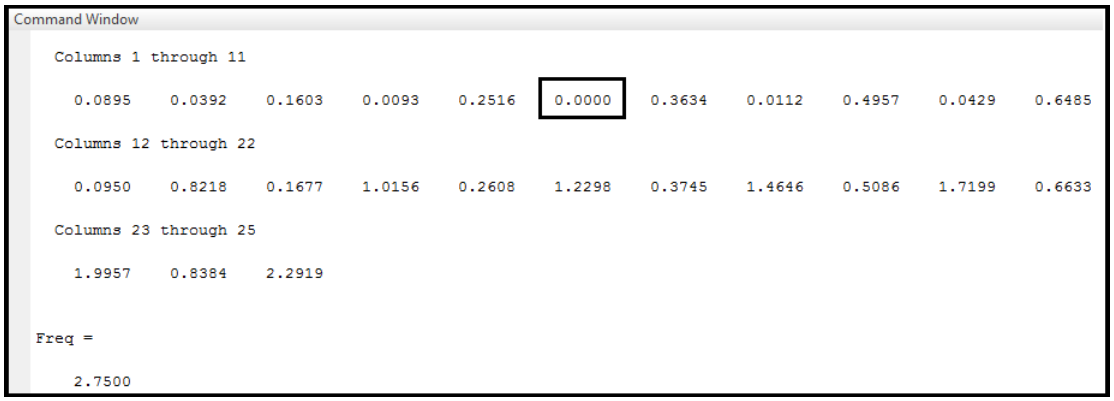

Figure 4.6. Unfolding the Original 2.75 GHz Signal. Using (2.6) to Compute the Scaled Lowest Slope Difference. Highlighted Value is the Likely Original Frequency Zone.

Test Three: 5.1 and 5.65 GHz Signals

The next test was a 5.1 GHz signal and a 5.65 GHz signal, which are some typical C-band radar frequencies. Each signal was applied separately and the results analyzed in MATLAB. The results are shown in Figure 4.7, which displays both signals in the $N = 0$ Nyquist zone. Comparing the signal slopes and modulation signals, we can extract the original frequency ranges. Adding the center frequencies from the results yields the original frequencies of the signals. Visible in Figure 4.7 are weaker images that appear to be signals; however, these are actually aliased signals from higher Nyquist zones folding down due to the wide bandwidth of the interpolation LPF. Reducing the LPF cutoff frequency to the upper limit of Nyquist zone $N = 0$ removes these artifacts.

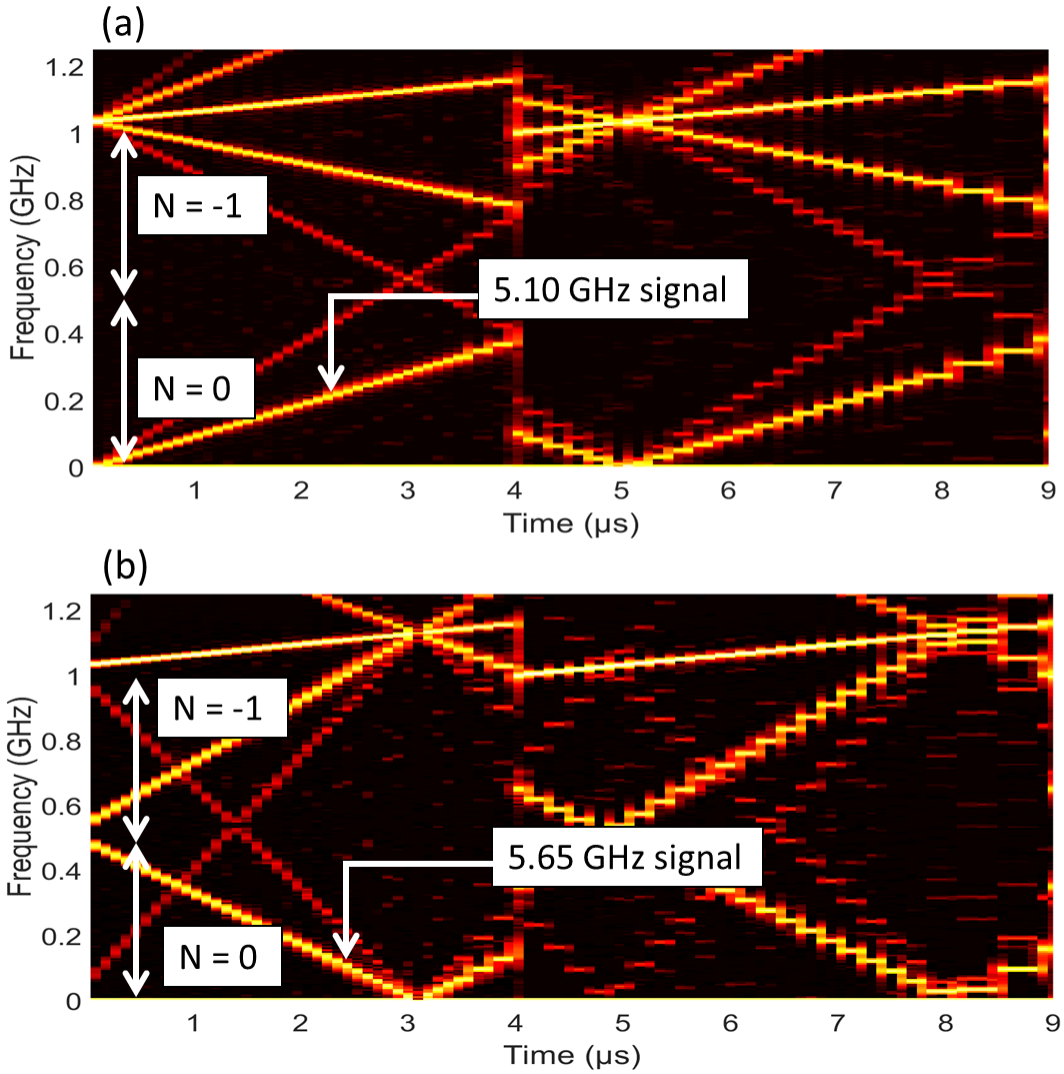

Figure 4.7. Test Three Results Displaying A) 5.10 GHz and B) 5.65 GHz Signals. Both Target Waveforms are Successfully Undersampled and Recoverable from the Spectrogram.

Test Four: 2.7 and 9.1 GHz Combination Signal

This test was conducted to determine how multiple target signals are resolved by the DM-NYFR simulation. Two target waveforms were applied to the antenna input: 2.7 GHz at 100 mV_{pp} and 9.1 GHz at 50 mV_{pp}. The uniform noise block was disconnected for this test. A spectrogram of the instantaneous optical power at MZI2's output is shown in Figure

4.8. Visible is the FM signal at 1.0 GHz and the modulated target signals in Nyquist zone $N = 0$. The antenna signals exhibit non-uniform aliasing expected from the NYFR, and two distinct signals are clearly identifiable. Given the slopes and center frequencies from the spectrogram, (2.6) and (2.7) can be used to successfully unfold the input RF signals to their original values.

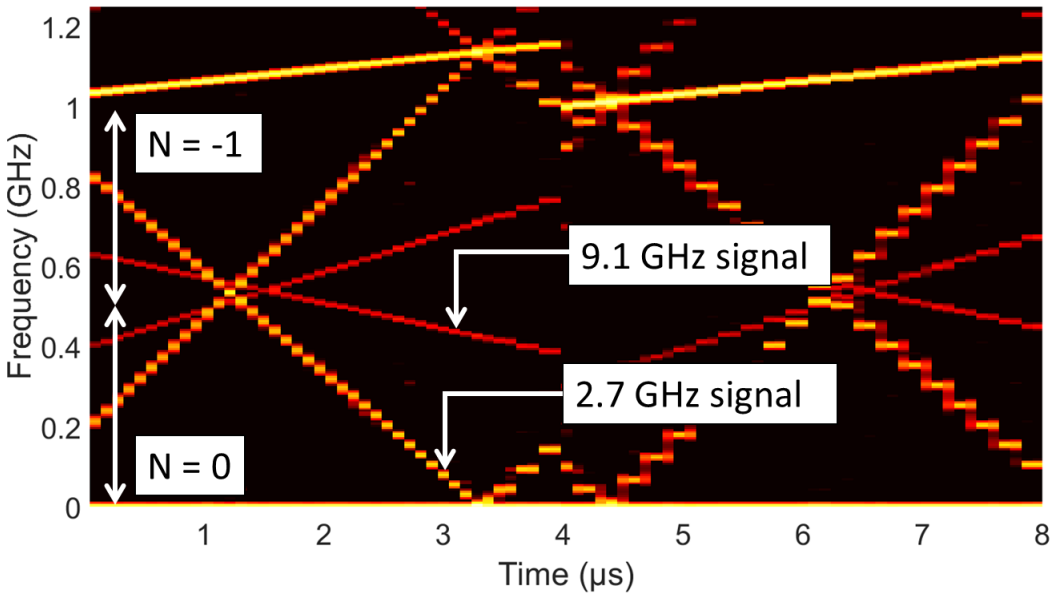

Figure 4.8. Test Four Results Displaying the Spectrogram of Folded 2.7 GHz and 9.1 GHz Signals

4.2 SM-NYFR Computer Simulation

The SM-NYFR uses a single MZI that acts as a carrier for the target signal. The compressed sensing is performed by an ADC triggered with a FM chirp signal described by (3.8). The rSoft simulation model is shown in Figure 4.9 and is comprised of an antenna block, signal modulation block, optical-to-electrical conversion stage, compressed sensing block, and FM sampling pulse generation. Individual components are listed in Table 4.2. The FM timing signal for the ADC results in a modulated sampling scheme which allows the compressed signal to be unfolded.

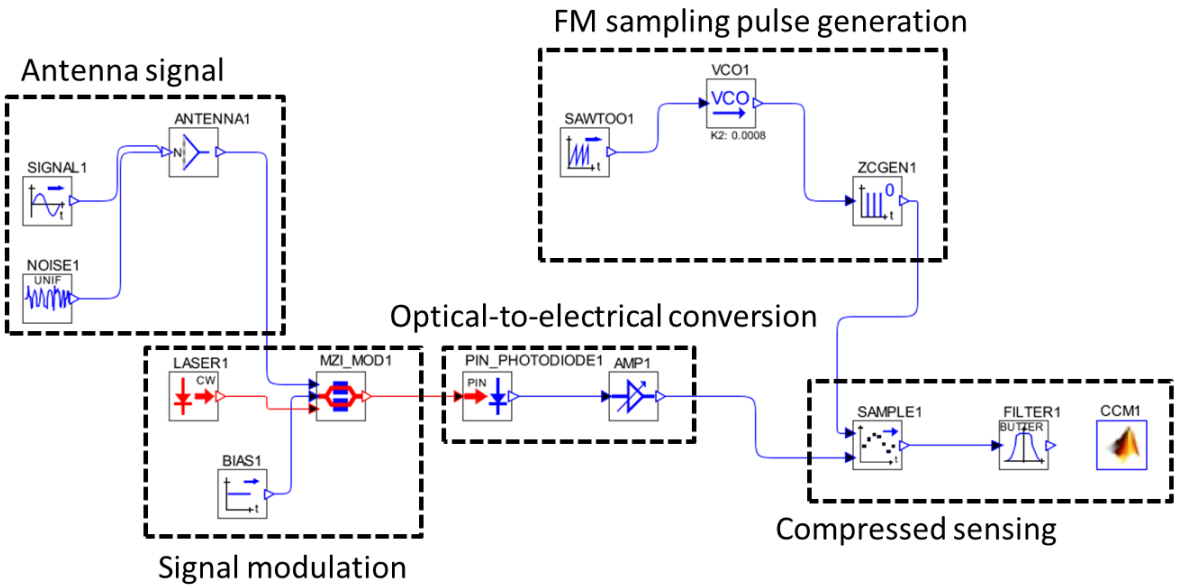

Figure 4.9. SM-NYFR Simulation Model with all Blocks Outlined

Table 4.2. SM-NYFR Component Labels, Names, and Descriptions from the SM-NYFR Computer Simulation Model.

Label	**Name**	**Function**
SAWTOO1	Sawtooth wave generator	Generates a electrical sawtooth wave from V_{min} to V_{max} that is fed into the VCO.
VCO1	Voltage controlled oscillator	Generates a linearly chirped sinusoid from the sawtooth input based on voltage sweep.
ZCGEN1	Zero crossing generator	Generates a picosecond wide electrical pulse every positive-to-negative zero crossing.
SIGNAL1	Electrical signal	Target RF signal.
NOISE1	Noise generator	Generates uniform electrical noise.
MZI_MOD1	MZI1	Modulates antenna signal onto CW laser
LASER1	Laser source	1550nm CW laser source.
PIN_PHOTO1	Photodiode	Converts an optical signal into an electrical signal.
SAMPLE1	ADC sampler	Converts analog signals to digital signals and is driven by ZCGEN1.

4.2.1 SM-NYFR Simulation Results

The simulations were conducted as described in Section 4.1.4. Testing was done to determine the performance of the SM-NYFR in comparison to the DM-NYFR. From test results, we see that the SM-NYFR has similar performance but a higher noise level with more artifacts in the results.

Test One: 5.25 GHz RF Signal

A 5.25 GHz signal was applied to the MZI electrode input and the results captured and exported to MATLAB. Two tests are run with the 5.25 GHz signal, the first with the VCO disconnected and no modulation present and the second with the VCO outputting a FM chirp to the zero-crossing generator to create an FM sampling pulse train used as an ADC trigger. The spectrogram of the 5.25 GHz signals are shown in Figure 4.10. From the results, we see Nyquist zone $N = 0$ and the modulated signal can be successfully unfolded to the correct frequency. The noise level appears higher than in the SM-NYFR results.

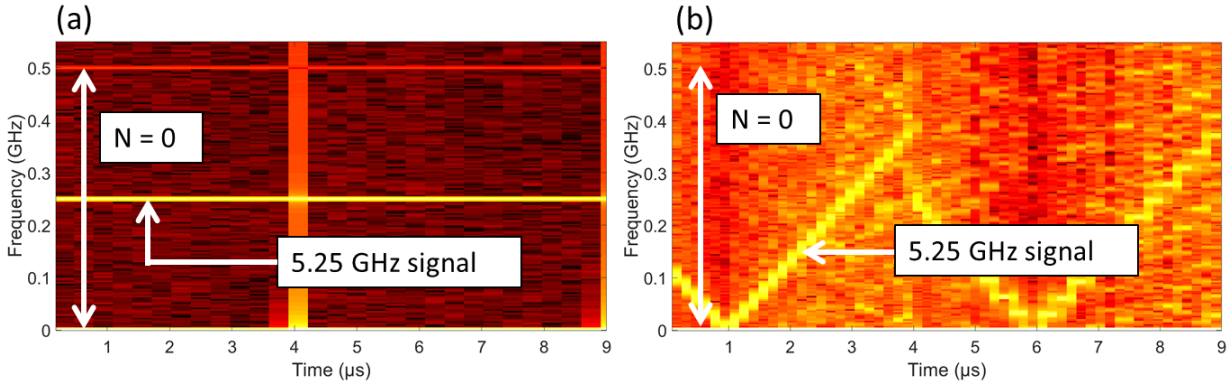

Figure 4.10. 5.25 GHz RF Results from an A) Unmodulated Sampling Signal and B) Modulated Sampling Signal

Test Two: 8.10 GHz RF Signal

For a second test, an 8.10 GHz signal was applied to the antenna input. The result is shown in Figure 4.11, and the original frequency was extracted. Unlike the DM-NYFR, from results we see large amount of noise clutter that could obscure a low signal-to-noise ratio signal such as an LPI waveform. This is indicated in Figure 4.11 by a label which marks an ambiguous area where the signal blends into the noise background.

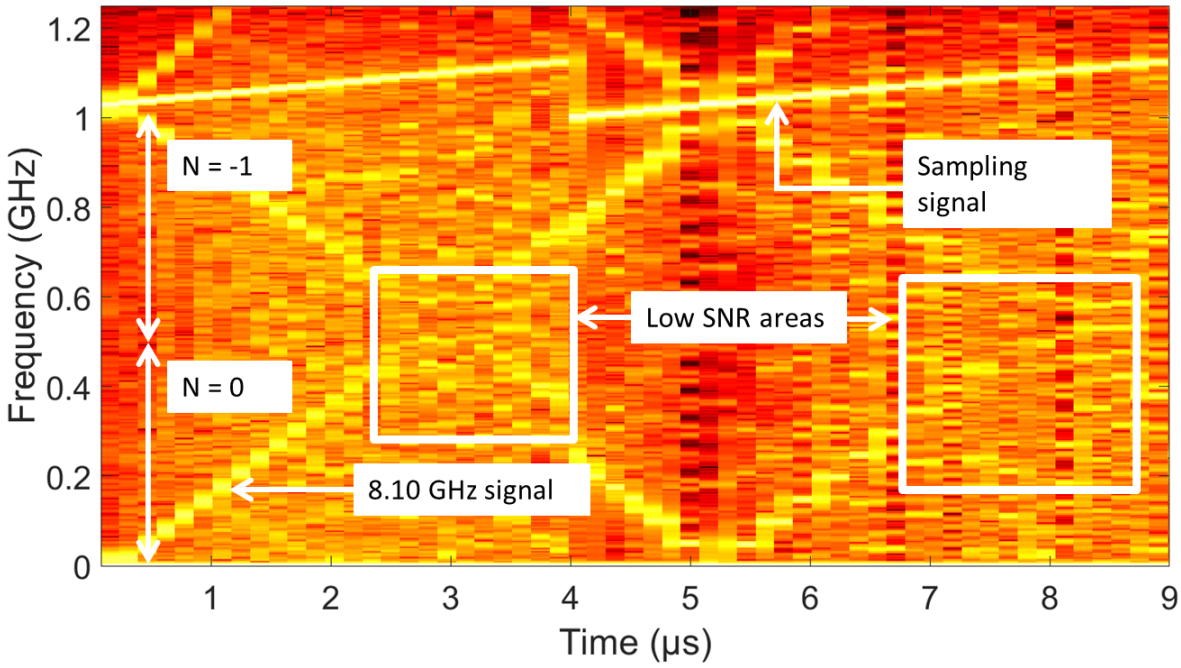

Figure 4.11. 8.10 GHz Target Signal Response. The High Noise of the SM-NYFR Design Makes Low SNR Signal Detection Difficult.

In summary, the computer simulations of the two receiver designs were discussed in this chapter. Both the DM-NYFR and the SM-NYFR architectures were modeled and simulated in order to test their operation. While both designs correctly unfolded compressed, incepted RF signals, the DM-NYFR design has a better noise response. The hardware prototype design of the DM-NYFR following the successful simulations is shown in the next chapter.

THIS PAGE INTENTIONALLY LEFT BLANK

CHAPTER 5:
Receiver Hardware Prototype Build

After successfully confirming the photonic NYFR designs in rSoft's OPTSIM design suite, a prototype NYFR was built to demonstrate physical operation. The design, construction, and testing of the hardware NYFR prototype and components are discussed in this chapter. Time constraints prevented building both the DM and SM architectures, and because the main focus of the research was on implementing integrated photonic compressed sensing techniques, only the DM-NYFR prototype was built in hardware. The principal challenge in constructing the hardware prototype was integrating commercial of-the-shelf (COTS) components in unique configurations that were not considered when the equipment was being manufactured. The hardware build makes use of components never intended for SIGINT or ELINT applications.

Additionally, component cost and funding was also a deciding factor during the prototype build. Due to funding limitations, lower cost equipment was used that did not meet the intended performance specifications of the designed or simulated architecture. Consequently, the prototype build is a scaled-down design that functions as a technology demonstrator and proof-of-concept rather than a fieldable receiver. Specifically, although the NYFR was designed and simulated to function in the GHz range with Nyquist zone bandwidths of 500 MHz, the hardware prototype is only able to operate in the kHz/MHz range with zone sizes of 50 kHz. Despite these constraints, the prototype is able to successfully undersample at sub-Nyquist rates and extract the original frequency information.

5.1 Overall Setup and Equipment Used

The DM-NYFR prototype build matches the block diagram in Figure 3.3 and is shown in Figure 5.1. The components list is shown in Table 5.1. The prototype uses a ThorLabs S1FC1550 1550 nm laser with an output power of 1.75 mW coupled into a JDSU X5 single-arm MZI with a DC bias to move the MZI out of positive quadrature as shown in Figure 3.2. The DC bias is set so that an applied electrode voltage of 0.0V will combine the MZI arms out-of-phase, and an electrode voltage of 5.5V will combine the beams in-phase. The X5 electrodes are attached to an electrical pulse generator (EPG) driven by an Agilent

E3612A DC power supply and Agilent 33220A 20 MHz function generator. The EPG is detailed in Section 5.3.

The MZI1 output is coupled to the MZI2 input, which is also a X5 modulator driven with another 33220A function generator which imitates an antenna input. The MZI2 DC bias is not used as the phase constant φ_o set during manufacture biases the modulator at positive quadrature. This allows the applied AC small signal to act on the most linear region of the MZI transfer function. The MZI2's output is connected to a Newport D-30IR detector. The detector's output is coupled with a Tektronix DPO4104 1.0 GHz digital oscilloscope which functions as an ADC and data collector, while a laptop computer running MATLAB performs the DSP. A ThorLabs EF502 filter is connected between the detector and the oscilloscope as an interpolation LPF with a 100 kHz cutoff frequency. All fiber used is SMF28E single-mode optical fiber.

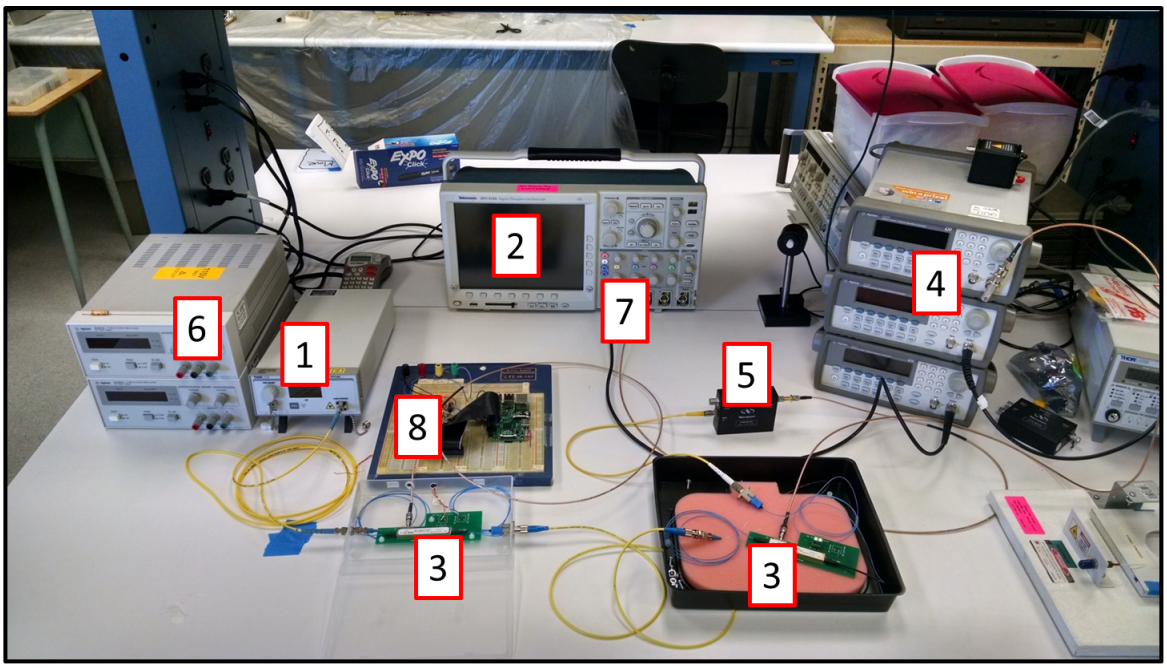

Figure 5.1. DM-NYFR Hardware Setup with Significant Components Numbered. The Components are Described in Table 5.1

Table 5.1. DM-NYFR Prototype Hardware Build Component Descriptions

Number	Part	Name	Function
1	S1FC11550	ThorLabs CW laser	1550 nm CW laser source outputting at 1.75 mW.
2	DPO4104	Tektronix scope	Digital 1 GHz oscilloscope used as an ADC and data collector when connected to a laptop.
3	X5-MZI	JDSU MZI	Single-arm MZI biased at zero for pulse generation and positive quadrature for signal inception. The MZI has a 40 GHz bandwidth. One is coupled with the EPG to generate sampling pulses, the other is coupled with the RF signal input. Switching voltage is $V_\pi = 5.5V$.
4	33220A	Agilent function generator	Programmable 20 MHz function generator. One is used to drive the EPG and another is used as an RF signal source.
5	D-30IR	Newport photodetector	PIN photodiode with an internal 10 dB LNA that converts optical signals into electrical signals.
6	E3612A	DC power supply	Power supply used to power to the EPG circuit.
7	EF502	ThorLabs LPF	100 kHz elliptical low pass filter (5th order) used as an interpolation filter between the detector and ADC.
8	EPG	Electrical pulse generator	Generates electrical pulses to drive MZI1. Design detailed in Section 5.3.

5.2 MZI Setup and Testing

The setup and testing of the MZIs used for modulating the CW laser is shown in this section. The JDSU X5 MZIs are mounted on silicon boards shown in Figure 5.2. Fiber attachments were soldered to the optical ports, and a coaxial cable attached to the RF input wire for the DC bias were attached to the MZI board. The MZI was mounted in a case to protect it from any physical damage.

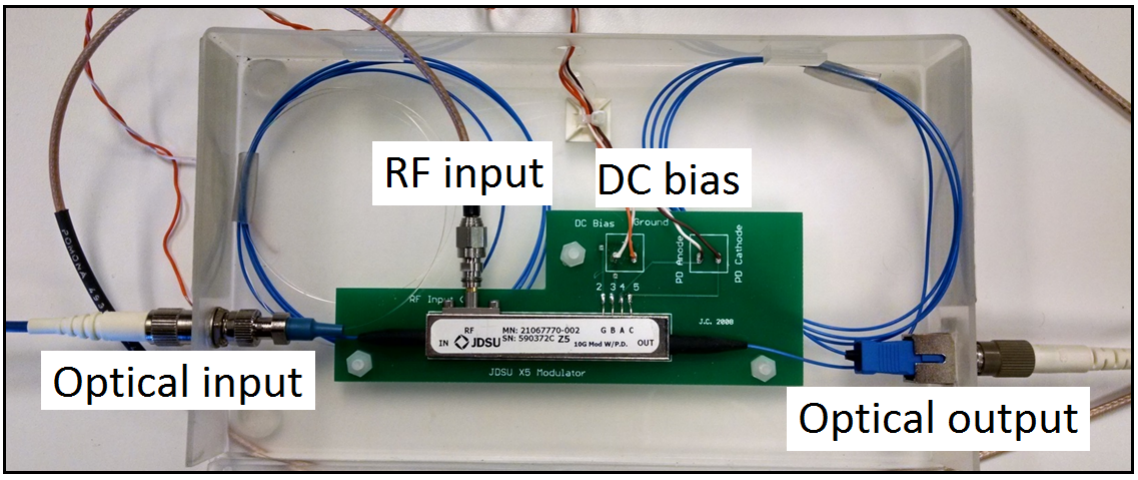

Figure 5.2. JDSU X5 MZI Mounted on a PCB Showing the RF Input, DC Bias, Optical Input, and Optical Output

The EPG circuit which outputs a 30.0-nanosecond wide electrical pulse at $V_\pi = 5.5$V was connected to the MZI, and an output optical pulse was examined in order to show the MZI response. The oscilloscope capture of the MZI optical output I_o is shown in Figure 5.3.

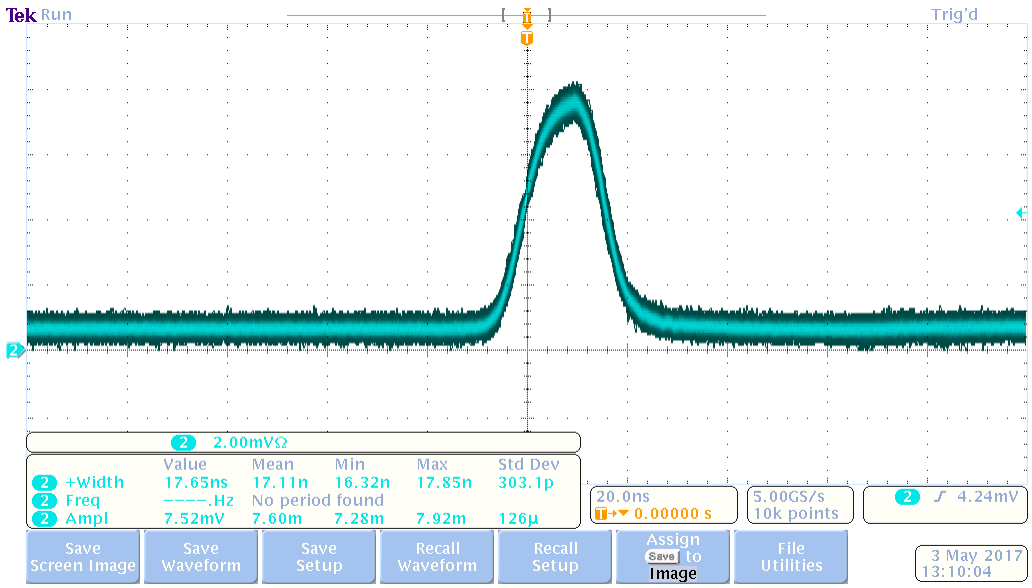

Figure 5.3. Oscilloscope Capture of a Single 30 ns Wide Electrical Pulse Incident on a JDSU X5 MZI

The -3.0 dB pulse width was measured as 17.11 ns at 7.60 mV. The pulse-width variance was 303.1 ps, and the amplitude jitter was 126.0 μV. The optical pulse width is smaller than the electrical pulse width due to the non-linear MZI input/output response (3.5).

5.3 Pulse Generation Circuit

An EPG circuit was built in the NPS photonics labratory using COTS components that can output a 30 ns wide electrical pulse train with an amplitude of 5.5V and a linear FM sweep as described in (3.8). The EPG is used to drive the first MZI and generate optical pulses sufficient for a prototype proof-of-concept build.

5.3.1 Circuit Design and Simulation

The EPG circuit was designed and simulated in NI Multisim, an electronic workbench built around SPICE software simulation to accurately model circuit behavior. The schematic is shown in Figure 5.4 along with a graphical representation of how a FM sinusoid propagates through the circuit. The EPG consists of three main parts: a swept sinusoidal AC source, a comparator, and a one-shot multivibrator.

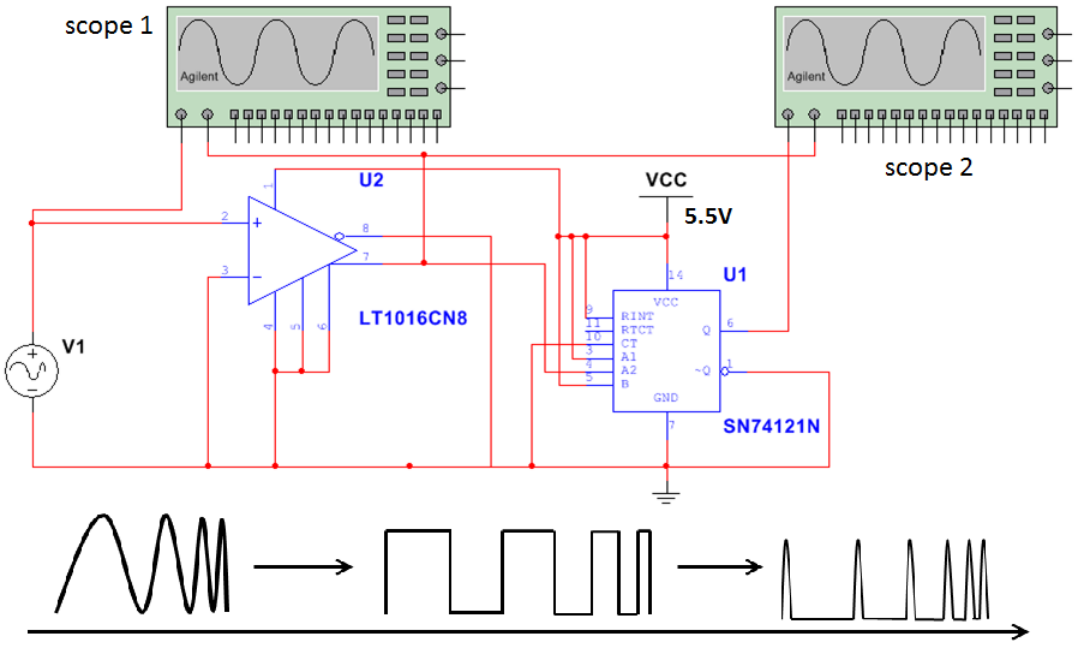

Figure 5.4. EPG Circuit Schematic Created in NI Multisim Along with an Example Waveform

Circuit Description

The AC source is a chirp waveform output from a 33220A signal generator which is connected to a LT1016CN8 comparator referenced to ground. The AC signal is V_1 and the reference level is V_2. When $V_1 \geq V_2$ the output is V_{cc}, 5.5V. Otherwise, the signal is grounded to 0.0V. This turns the chirp sine wave into a swept-square wave with distinct rising and falling edges. These edges are used as triggers for the pulse generator. The LT1016 has unused reference pins that must be grounded in order to function correctly. The trigger signal from the comparator is sent to the SN74121N monostable one-shot multivibrator that outputs the electrical pulses.

The SN74121N is a voltage oscillator that can flip between two states, V_{cc} and ground, when triggered by a clock edge. Only the ground state is stable, however, and the high state is unstable. A falling edge trigger pushes the multivibrator into the unstable state, setting the output high for a specific time determined by a programmable RC constant τ. For the EPG, τ=30 ns, and because the swept-square waveform functions as the trigger signal,

every falling edge outputs a 30 ns wide electrical pulse with an amplitude of $V_\pi = 5.5$V.

NI Multisim Test

The schematic shown in Figure 5.4 was simulated in NI Multisim, and the results are shown in Figure 5.5. The SPICE models for the SN74121N and LT1016CN8 were downloaded and imported from an NI chipset database. The AC signal input and comparator output is shown with scope 1 and tests the square-wave conversion. The falling edge trigger from the LT1016 and a single 30 ns wide pulse is displayed by scope 2. The output has a perfect impulse shape due to the simulation parameters not including a realistic load.

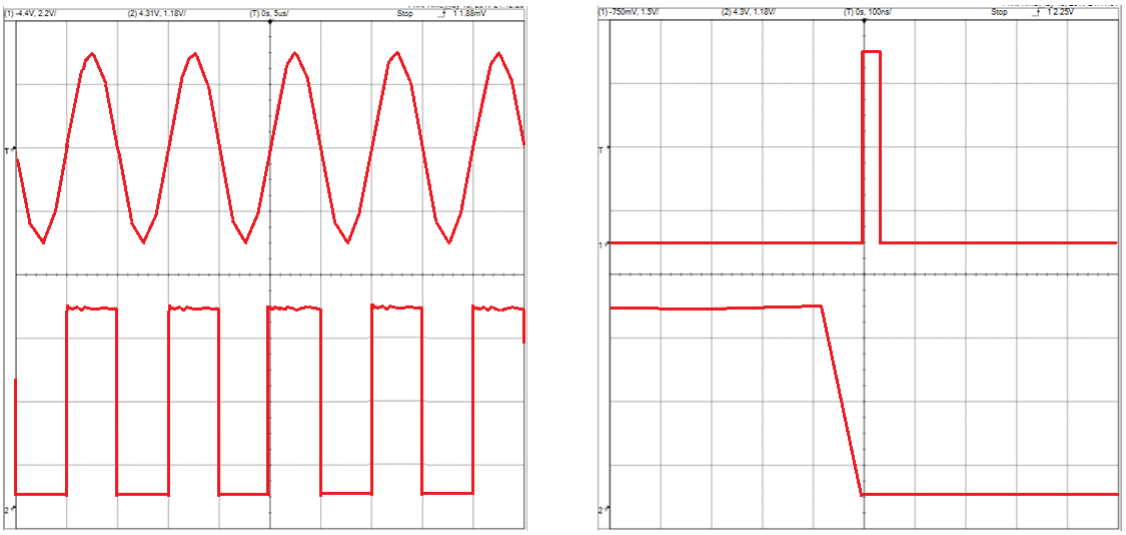

Figure 5.5. Multisim Simulation Showing the Output of Scope One and Two

5.3.2 Pulse Generation Testing

The EPG circuit in Figure 5.4 was constructed on a breadboard for testing. The input was attached to a 1.0 MHz sine wave and the output connected to the test bench. An oscilloscope was used to probe various points of the circuit in order to test all the parts and confirm overall function. The oscilloscope outputs are shown in Figure 5.6. Shown in Figure 5.6(a) are probes connected to the input and output of the LT1016 converting the sinusoid into a clock signal. Additionally, the SN74121 functionality is demonstrated by

capturing the input clock signal and the output pulses, which are confirmed to be 30 ns long and are shown in Figure 5.6(b).

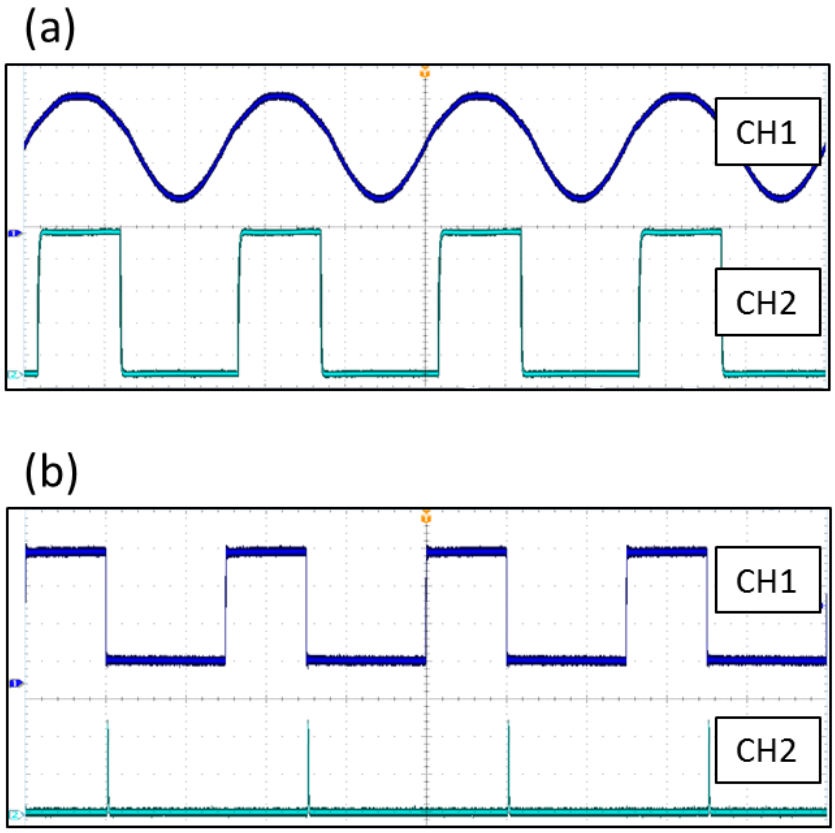

Figure 5.6. Results of EPG Testing A) Clock Signal Generation with CH1 Connected to the Input FM Sweep and CH2 Connected to the LT1016 Output and B) Pulse Generation with CH1 Connected to SN74121 Input and CH2 Connected to the EPG Output

A detailed examination of a single falling edge and timing pulse is shown in Figure 5.7. These tests indicate the EPG circuit is functioning correctly. Lastly, the oscilloscope is attached to measure both the output electrical pulses and the output optical pulses. The MZI is coupled with a PIN photodiode in order to measure the optical pulses by converting them into electrical signals. This is shown in Figure 5.8 with both the electrical pulses and their corresponding optical pulses. The optical pulses slightly lag the electrical pulses, but otherwise, the MZI output response mimics the driving signal.

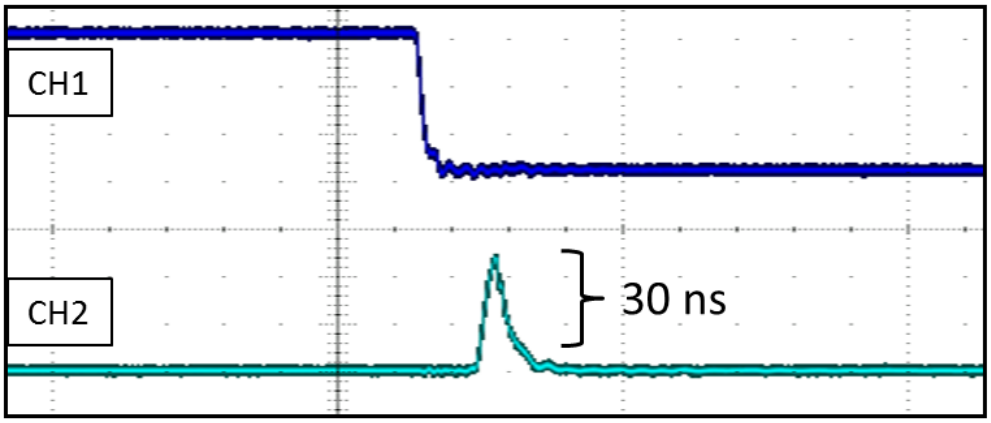

Figure 5.7. Single Falling Edge (CH1) with Electrical Pulse (CH2)

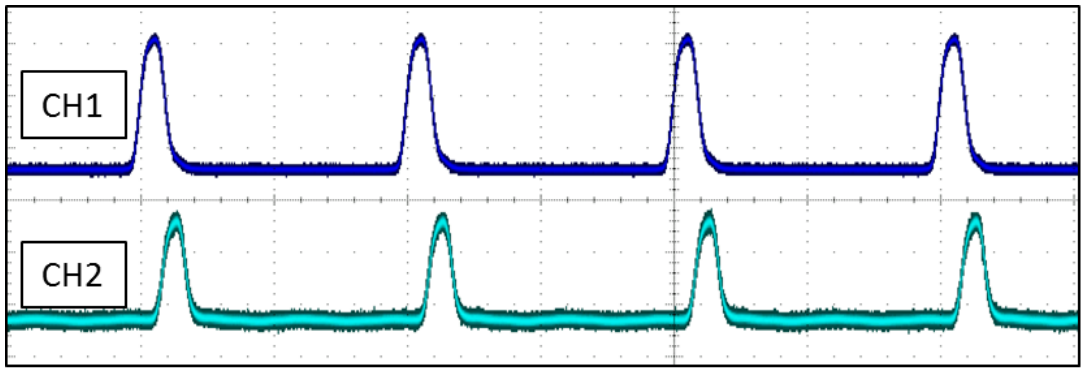

Figure 5.8. Electrical Pulses (CH1) and the Corresponding Optical Pulses (CH2)

The design, construction, and testing of the hardware NYFR prototype and components was discussed in this chapter. The prototype used COTS components to implement a scaled down photonic NYFR that functions as a proof-of-concept build. Testing confirmed the individual components and their functionality. Test results from the functioning NYFR prototype with target RF signals is detailed in the next chapter.

THIS PAGE INTENTIONALLY LEFT BLANK

CHAPTER 6:
Prototype Test and Evaluation

The hardware prototype testing, evaluation, and results of the DM-NYFR shown in Figure 5.1 is covered in this chapter. Multiple modulation schemes are tested with the first MZI stage to confirm the FM optical pulse train output. The primary results are from time-frequency spectrogram captures of target signals from the RF signal generator. Additionally, the signal processing methodology of de-noising, thresholding, and edge detection which made the incepted signals human readable is discussed in this chapter.

6.1 FM Optical Pulse Testing

Four FM presets are used as modulation schemes for the sampling pulse train. The FM presets are listed in Table 6.1 where t_m is the modulation period, ΔF is the sweep bandwidth, and f_c is the starting frequency for the sweep. All modulations are linear sawtooth chirps instead of triangular chirps, which were chosen due to hardware limitations with the signal generator. The varying bandwidths of the FM chirp signal presets allows a wide spectrum of target RF waveforms to be folded by the NYFR. Higher frequency signals are intercepted more efficiently with smaller sweep bandwidths, whereas larger sweep bandwidths perform better for lower frequency signals. The relationship between sweep bandwidth and compressed signal bandwidth is explored in detail in Section 6.3 along with the effects of using a non-ideal modulation sweep bandwidth preset.

Table 6.1. Pulse Train FM Presets

Preset	**Parameters**
Preset 1	t_m = 2 ms ΔF = 25 kHz f_c = 100 kHz
Preset 2	t_m = 2 ms ΔF = 15 kHz f_c = 100 kHz
Preset 3	t_m = 2 ms ΔF = 10 kHz f_c = 100 kHz
Preset 4	t_m = 2 ms ΔF = 5 kHz f_c = 100 kHz

Oscilloscope captures are used to analyze the pulse-repetition interval (PRI) over a modulation sweep. This is shown in Figure 6.1, which highlights the changing PRI at the beginning of the modulation sweep and near the end of the modulation sweep. A PRI of 0.01 ms corresponds to the starting frequency of 100 kHz, while the PRI of 0.0081 ms corresponds to a repetition frequency of 123.46 kHz.

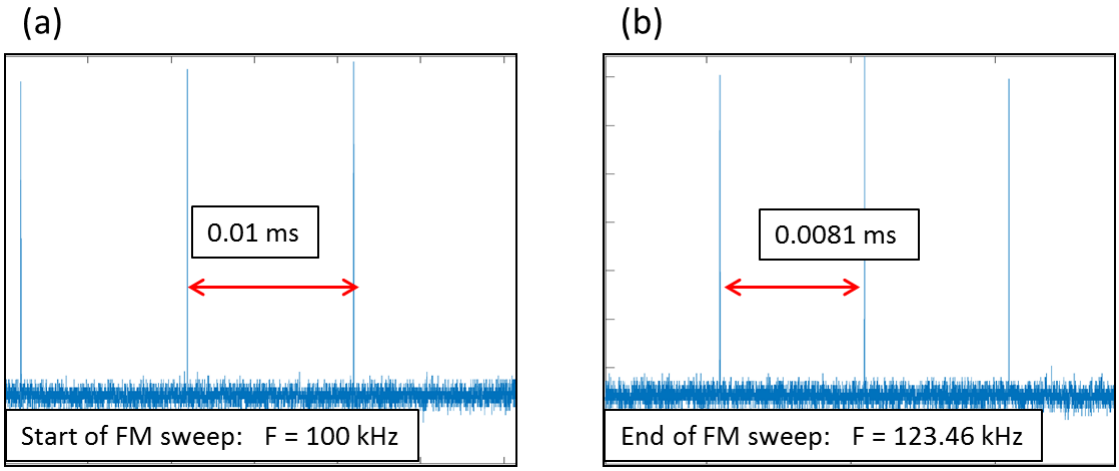

Figure 6.1. FM Optical Pulse Train PRI Measured at A) Beginning of the Sweep and B) Near the End of the Sweep

Additionally, the captured oscilloscope output was analyzed in MATLAB in order to plot a time-frequency representation of the optical pulse train. The results are shown in Figure 6.2, which overlays the time-domain oscilloscope capture with the frequency-domain spectrogram to show the modulation bandwidth of 25 kHz. The test result confirmed the operation of the optical pulse generation circuitry when the input signal is linearly chirped.

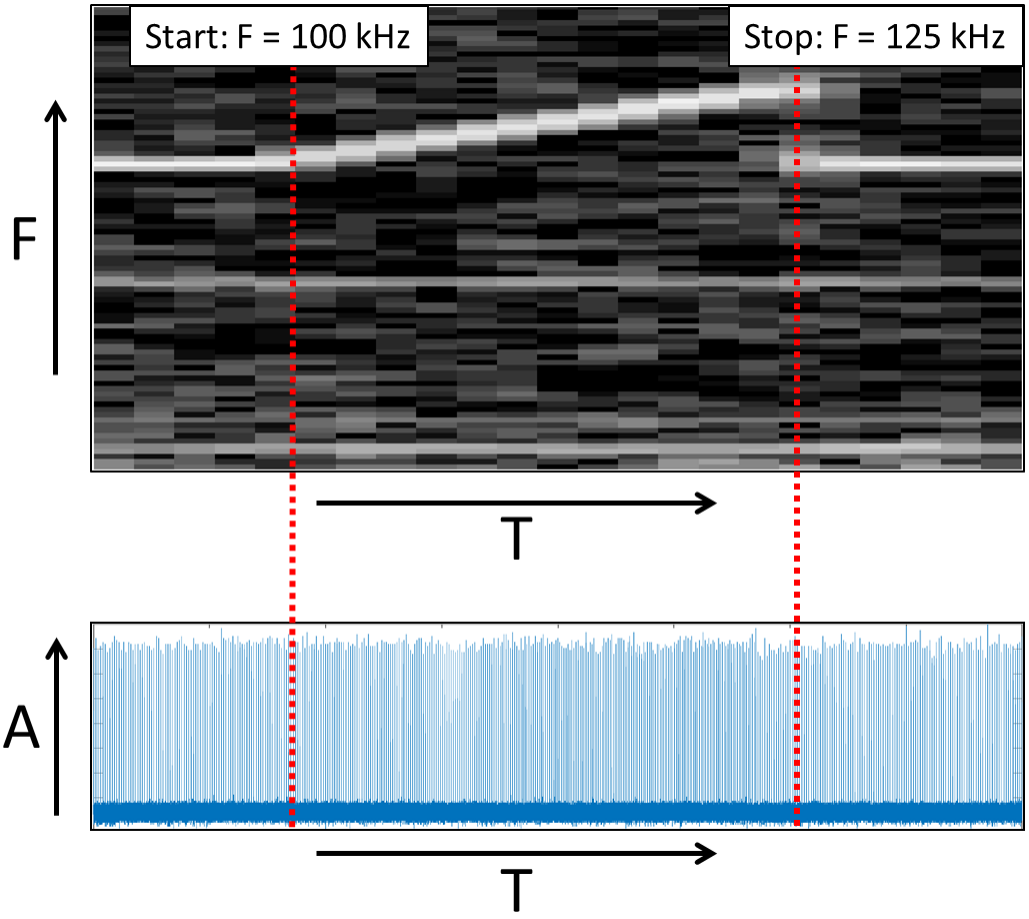

Figure 6.2. Time-Frequency Spectrogram of FM Optical Pulses Compared Against Amplitude-Time Oscilloscope Capture

6.2 Signal Processing Methodology

The signal processing methodology, specifically noise removal and thresholding, that is required due to the high noise floor of the optical signals is covered in this section. This is due to the low optical power on the input of MZI2 as well as characteristics associated with the MZI functionality. Each MZI has roughly a 3 dB loss between the input optical intensity and the output optical intensity. As the modulators are added in series, power loss increases, resulting in low incident power on the detectors. Another factor for the high noise floor when using MZIs is the imperfect extinction ratio that prevents total destructive interference. The ideal case of the MZI transfer function is illustrated in Figure 3.2; however,

in actual operation it is impossible to completely reduce the output intensity to zero and as a result some laser output is always present. Lastly, relative intensity noise (RIN) arises from power instabilities and vibrations within the CW laser cavity. With a low sampling signal duty cycle, the time-averaged noise power is larger than the signal power, and de-noising is a necessity. This is shown in Figure 6.3.

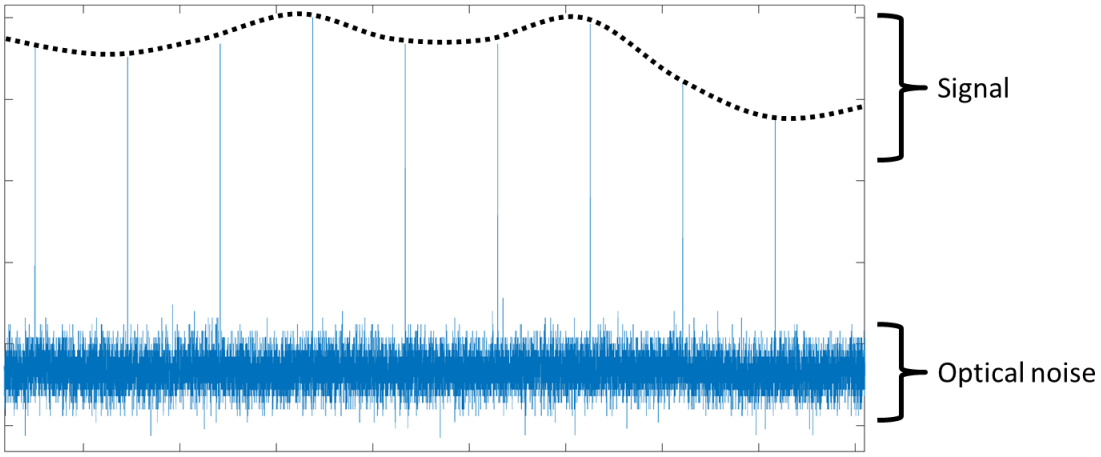

Figure 6.3. Example NYFR Capture Illustrating Both the Signal and Optical Noise.

The folded signal includes optical noise which needs to be filtered before analysis can take place. Additionally, thresholding and edge detection are implemented to make the undersampled signals distinguishable. The image processing block diagram is shown in Figure 6.4 and details the DSP steps to refine the NYFR output.

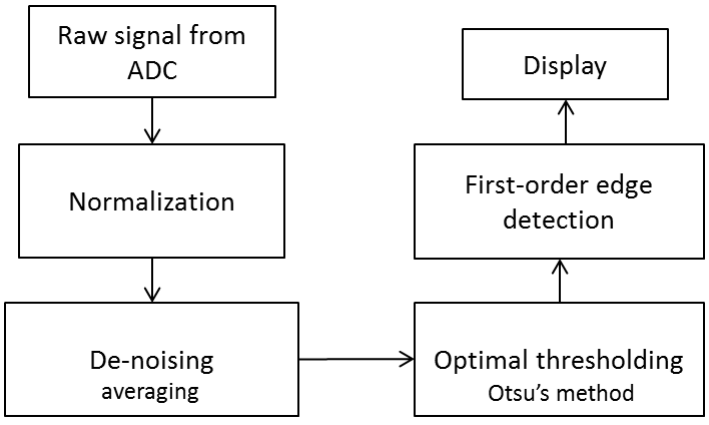

Figure 6.4. Block Diagram of NYFR Image Processing Steps

The raw ADC signal is first normalized and then passed into a noise removal block that uses squared averaging to compute a cutoff value below which the signal is set to zero. The noise power P_{noise} is defined as

$$P_{noise} = \frac{\sum_{i=1}^{n} \left(S[i] - \bar{S}\right)^2}{n} \tag{6.1}$$

where $S[i]$ is the n sized signal array and i is the index corresponding to a data point. The signal is de-noised by setting the signal array to

$$S[i] = \begin{cases} S[i] & \text{if } S[i] \geq P_{noise} \\ 0 & \text{if } S[i] < P_{noise} \end{cases} \tag{6.2}$$

which removes much of the optical noise. After initial processing, the signal is thresholded in order to facilitate edge detection. Otsu's method of optimal thresholding is used to isolate the signal from the background noise by identifying the 0th and 1st order cumulative moments of an n-sized histogram. The maximum variance of the class separability between the two histogram moments is the optimal thresholding point [16]. This is shown graphically in Figure 6.5, which is a histogram of a NYFR capture with Otsu's point labeled. Lastly, a simple edge detection method used binarization to convert the signal into a two-state array depending on the average power after thresholding. Anything less than the average power after thresholding was set to zero, which highlighted the folded signal slope. All signal processing steps were implemented with MATLAB. As a result of the signal processing steps, both the MZI optical noise and RIN was effectively removed from the ADC captures and the signals were able to be correctly unfolded.

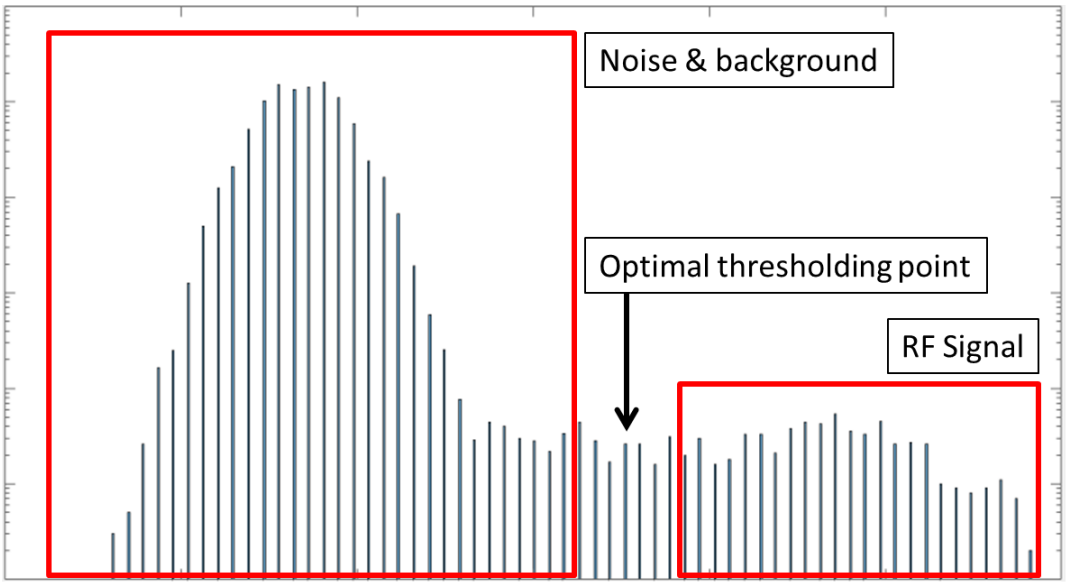

Figure 6.5. Example NYFR Capture Histogram Illustrating Otsu's Method of Optimal Thresholding

6.3 Single-Tone Test Results

Selected DM-NYFR tests using a single frequency tone as the target RF signal are shown in this section. The sampling modulation presets used are listed in Table 6.1. Target RF signals are successfully undersampled and extracted using DSP, confirming the prototype's functionality.

6.3.1 Selected Tests

Select tests with full DSP methodology are presented in this subsection in order to highlight the NYFR functionality. The first selected test was a 225 kHz RF signal with preset three as the modulation scheme. The results are shown in Figure 6.6, which details both the final signal and the image processing steps. All displays are time-frequency spectrograms computed in MATLAB showing a full ΔF frequency sweep and Nyquist zones $N = 0, -1$. The capture in Figure 6.6(a) is the raw received signal from the ADC block of the NYFR. The 225 kHz signal is masked by noise and is not discernible from the image. In Figure 6.6(b) we see the DM-NYFR signal after preliminary de-noising and normalization. At this stage the target signal is faintly visible from the background. The next capture, Figure

6.6(c), is after the application of optimal thresholding, which removes almost all of the clutter and leaves the target signal clearly identifiable. Figure 6.6(d) is an illustration of the final output of the DSP block and is used in conjunction with the unfolding methodology described in Section 4.1 using (2.6) and (2.7). This is shown in Figure 6.7 as a red line fit to the slope of the signal, which was used to successfully extract the correct original frequency of the target RF waveform.

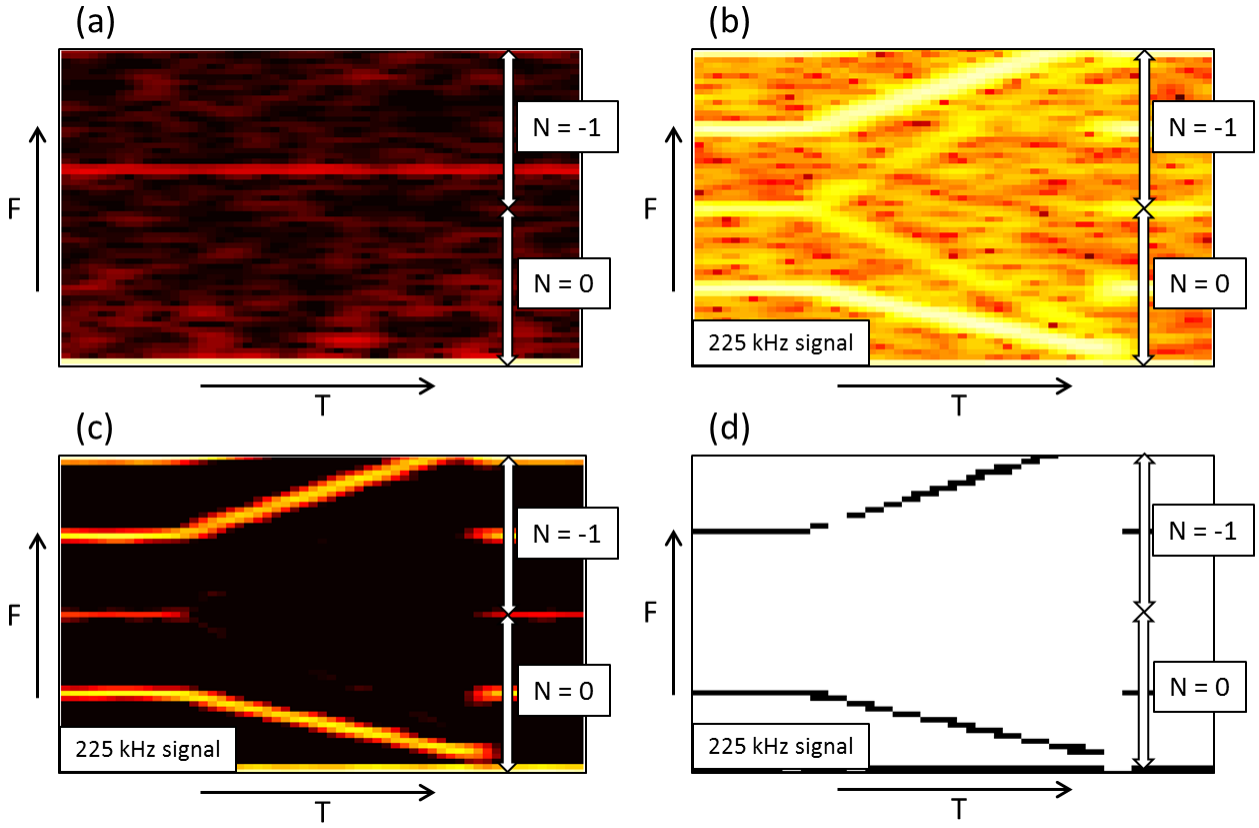

Figure 6.6. 225 kHz Test with Preset Three Showcasing the DSP Steps: A) is the Raw ADC Signal, B) is the Initial De-Nosing and Normalization, C) is the Optimal Thresholding, and D) is the Final Signal After Edge Detection.

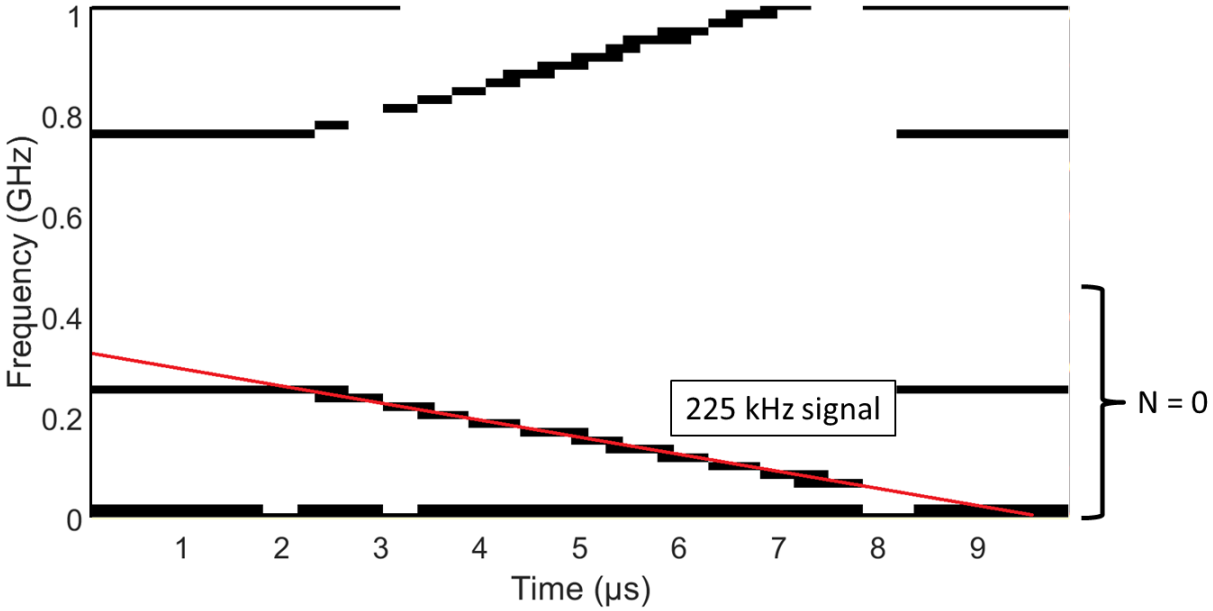

Figure 6.7. 225 kHz Signal with a Fitted Slope for Unfolding

The second selected test was a 525 kHz RF signal with preset four as the modulation scheme and is shown in Figure 6.8 as a series of time-frequency spectrograms. The results confirm the NYFR's operation by replicating the 225 kHz test. Clear progression is shown through each DSP block culminating in a distinguishable signal that is unfolded into its original Nyquist zone. Interestingly, in Figure 6.7(a) we see the same weak tone signal in Nyquist zone $N = -1$ that is present in Figure 6.6(a). This single frequency anomaly is not associated with any target signal and disappears when the noise is removed. This tone likely arises from a periodic oscillation in the optical noise stemming from the MZI. The modulators have a cosine-squared pattern transfer function as described in (3.3), which causes spurious frequencies. Another explanation is laser RIN vibrations resonating in the laser cavity. Although this does not appear to affect the DM-NYFR performance, these tones did not appear in the rSoft simulations, and this underscores the importance of hardware prototyping.

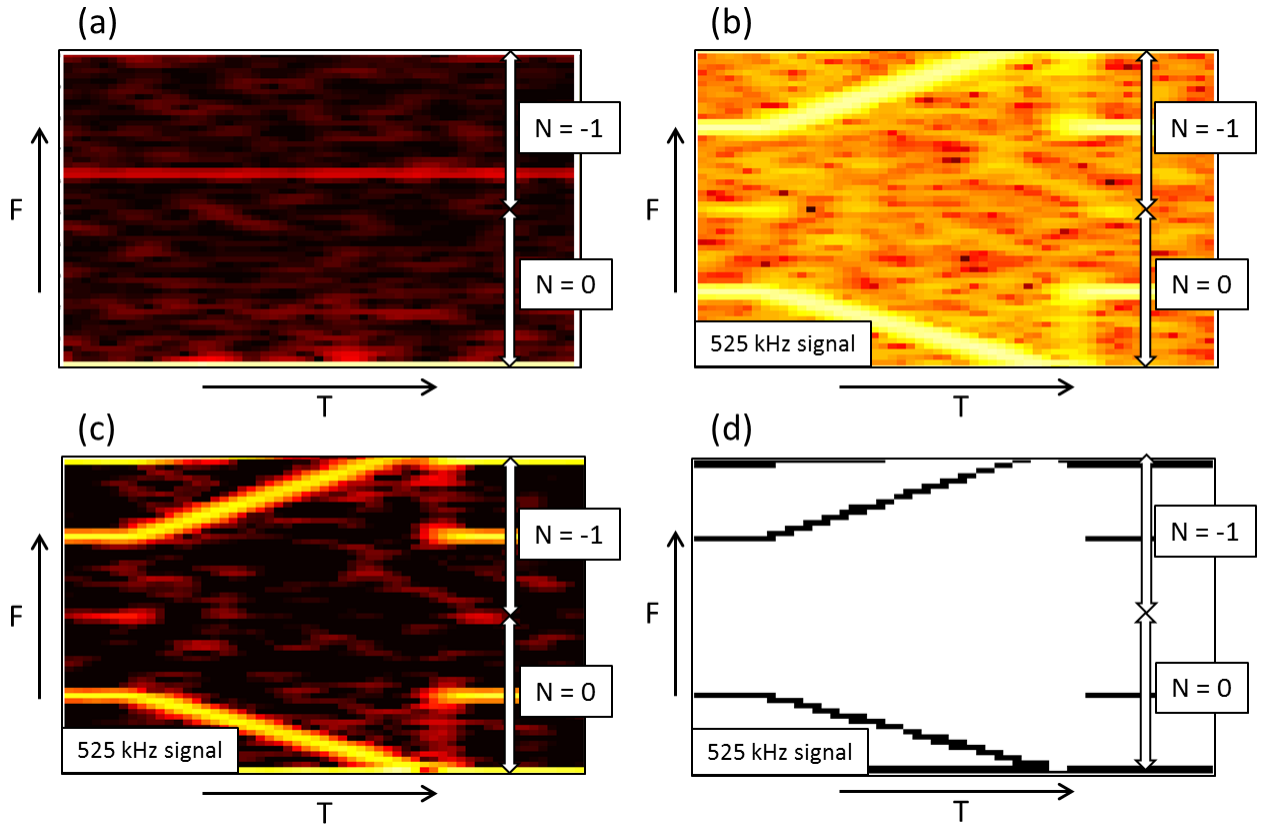

Figure 6.8. 525 kHz Test with Preset Four Showcasing the DSP Steps: A) is the Raw ADC Signal, B) is the Initial De-Nosing and Normalization, C) is the Optimal Thresholding, and D) is the Final Signal After Edge Detection.

The modulation sweep bandwidth ΔF has a direct affect on the output modulation slope and can adversely alter the results. A common occurrence when dealing with a large modulation slope is Nyquist zone overflow. The imparted modulation S_m is modeled as

$$S_m = f_c + M\Delta F \tag{6.3}$$

where f_c is the center frequency of modulation, ΔF is the sweep bandwidth, and M is a scale factor from the original signed Nyquist zone. As a result, S_m grows as either the target RF frequency or modulation sweep increases. This can cause an overflow effect where a signal modulation crosses the bounds of a Nyquist zone, changing the slope value and sign. Depending on the capture size, we can detect and account for this overflow. This is shown in

Figure 6.9, where a 425 kHz signal is modulated with a 10 kHz ΔF. The overflow is evident at the 1.75 ms point, when the slope reflects back into the $N = 0$ Nyquist zone; however, due to the capture size of 4.0 ms, this was detected and corrected. It is recommended that the capture time t_c is at least twice the modulation time t_m such that $t_c > 2t_m$.

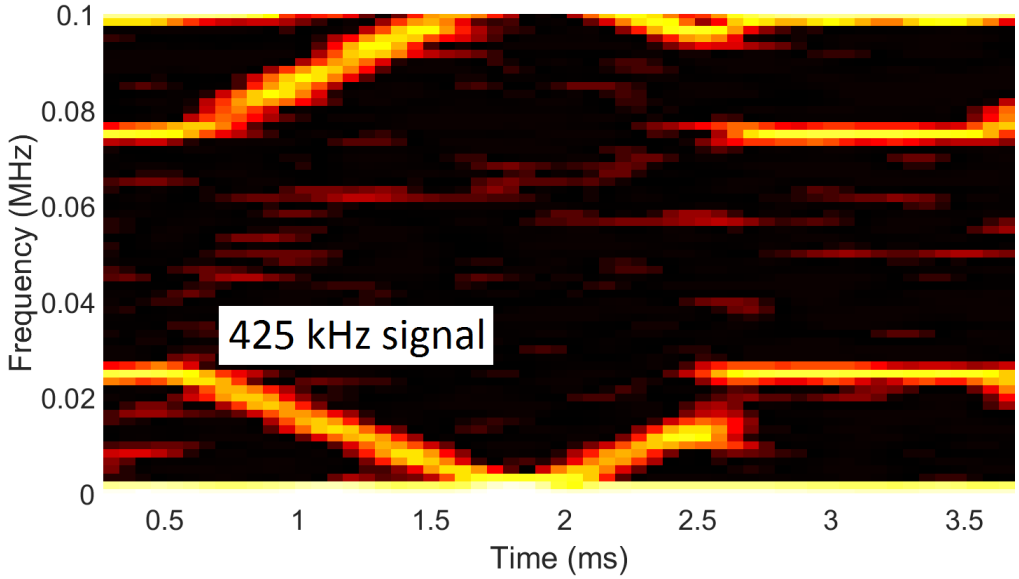

Figure 6.9. Nyquist Zone Overflow at 1.75 ms

The hardware prototype testing and results for RF target signals was discussed in this chapter. The DM-NYFR functioned correctly, and applied signals were successfully unfolded into their correct original frequencies. This prototype, while not a fieldable design, serves as a proof-of-concept for photonic NYFR compressed sensing. The thesis conclusions and potential future work are discussed in the next chapter.

CHAPTER 7:
Conclusion and Future Work

The thesis results and future directions for further research are discussed in this chapter. Despite limitations on the physical prototype, the photonic NYFR architecture was successful, both in simulations and hardware, in sensing signals above of the traditionally required Nyquist rate.

7.1 Conclusion

In conclusion, this thesis research was successful in answering the question of whether integrated photonic components can be used to construct a novel compressed sensing receiver. Over the course of this thesis research, we implemented the NYFR architecture in the photonic domain, taking advantage of the increased bandwidths, sampling speeds, sensitivities, and EMF noise immunity that optical devices possess. Two potential design architectures, the DM and SM NYFR, were designed during the research. The SM-NYFR was primary envisioned as a technology demonstrator, while the DM-NYFR is the principal research contribution. The primary motivation for this thesis was to implement a novel undersampling technique with photonic components in order to take advantage of the large bandwidths of optical devices. This enables direct digitization and analysis of wideband signals from the RF spectrum.

The design was successfully simulated in OPTSIM in order to confirm functionality. Computer simulations showcased the photonic NYFR's ability to detect and recover signals an order of magnitude larger than the sampling frequency. The DM-NYFR uses two optical modulators. The first generates an FM optical impulse train, and the second incepts the signal as an envelope. The pulses are generated with an EPG outputting V_π amplitude 30-ns wide pulses triggered every falling clock edge. The clock is frequency modulated with the specific NYFR scheme. After the signals are modulated, they are coupled into a PIN photodiode sampled by an ADC at the Nyquist rate of $2\omega_s$. Digital signal processing de-noised and thresholded the signals, which were then unfolded to recover their original Nyquist zone. Results with the hardware prototype show proof-of-concept and confirm the NYFR architecture. Target signals tested included both single tone and pulsed RF

waveforms outside of the Nyquist criterion, which were successfully unfolded.

7.2 Future Work

Suggested future work should focus on improving the hardware prototype beyond a proof-of-concept design. The primary limitations come from the COTS design of the pulse-generation mechanism. Described in Sections 3.4.2 and 3.4.3, the optical pulse width of MZI1 is the biggest limiting factor that determines the NYFR upper interception frequency. Current EPGs can output high fidelity picosecond-wide pulses that can enable GHz-range target RF signals. Another pulse generation technique is to use mode-locked lasers to generate short optical pulses. Mode-locked lasers are commonly used to generate impulse trains; however, the time it takes for the laser to settle generally precludes frequency modulating the pulses. Novel PRF sweeping with mode-locked lasers should be explored further.

Additional research directions include integrating the photonic NYFR with current photonic direction finding capabilities in order to develop a comprehensive wideband SIGINT/ELINT platform that would not only provide NYFR compressed sensing but also line-of-bearing (LOB) directional capability. Investigating a parallel channel configuration would allow multiple signal modulations per capture and would generate more information to unfold the signal. Using the NYFR as the front-end receiver, we could integrate with the wideband antenna system at L3 Technologies and implement autonomous signal classification and parameter extraction to test the photonic NYFRs capability in an integrated system. Lastly, implementing the photonic systems with superconducting quantum interference device (SQUID) modulators would improve the photonic NYFR sensitivity.

APPENDIX: MATLAB Code

```
 Nyquist Zone Code
 Richard Shmel, NPS
 computes the Nyquist zone from the slopes of the signal and modulation
--------------------------------------------------------------------------------

M = [0,-1,1,-2,2,-3,3,-4,4,-5,5,-6,6,-7,7,-8,8,-9,9,-10,10,-11,11,-12,12];
Mf = [0,.5,1,1.5,2,2.5,3,3.5,4,4.5,5,5.5,6,6.5,7,7.5,8,8.5,9,9.5,10];
Mx = [0,-1,2,-3,4,-5,6,-7,8,-9,10,-11,12,-13,14,-15,16,-17,18,-19,20,-21];

rx notes
rfx1 = 4.594e-6;
rfy1 = 1.019e9;
rfx2 = 5.906e-6;
rfy2 = 1.061e9;
S_clk = (rfy2-rfy1)/(rfx2-rfx1); %slope of the clock

Signal
sigx1 = 0.4688e-6;
sigy1 = 0.1387e9;
sigx2 = 1.688e-6;
sigy2 = 0.368e9;
center_freq = 0.15;
S_sig = (sigy2-sigy1)/(sigx2-sigx1); %slope of the radar pulse (ie, rise/run)

NYQUIST unfolding
equations from section 2
[X] = (S_sig-Mf*S_clk).^2
[A,I] = min((S_sig-Mf*S_clk).^2);
Nz = Mf(I);
Nzf = Mf(I);
Freq = Mf(I)+center_freq
```

```
 Spectrum results
 Richard Shmel
 imports results and runs some basic de-nosing and thresholding
 described in section 6
--------------------------------------------------------------------------------
 import file
clear
s1='C:\Users\*\Desktop\PNYFR\v4\';
s2='325k_5';
s3='.csv';
s = strcat(s1,s2,s3);
[X,Y] = importfile(s,14, 1000013);
fs = 160e9;
N = 150000;
fs = 250e6;

 thresholding value from historgram
thresh = hist_out;
ax_l = 0.0;
ax_h = 0.1;
load('cmap.mat');

figure(1)
hold on
colormap(hot)
axis([-inf inf ax_l ax_h])
spectrogram(Y,hamming(N),9*N/10,N,fs,'yaxis')
savefig(strcat('*\Fold_test_1\',s2,'_raw'));
hold off

norm = max(Y);
Y = (Y./norm)*5;
new_max = max(Y);
Y(Y<1.5)=0;
```

```
figure(2)
hold on
colormap(hot)
axis([-inf inf ax_l ax_h])
spectrogram(Y,hamming(N),9*N/10,N,fs,'yaxis')
savefig(strcat('*\Fold_test_1\',s2,'_denoise'));
hold off

figure(3)
hold on
colormap(hot)
axis([-inf inf ax_l ax_h])
spectrogram(Y,blackmanharris(N),9*N/10,N,fs,'MinThreshold',thresh,'yaxis')
savefig(strcat('*\Fold_test_1\',s2,'_thresh'));
colorbar off;
hold off
```

```
 FMCW GEN
 Richard Shmel
 generates an FMCW sawtooth waveform to output to signal generator
 I&Q matrix
 can change bandwidth, period, and cycles
--------------------------------------------------------------------------------

sFMCW = phased.FMCWWaveform('SweepBandwidth',20e6,...
'SampleRate',100e6,'SweepDirection','up',...
'NumSweeps',1,'SweepTime',10e-6);
sig = step(sFMCW);
windowlength = 16;
noverlap = 64;
nfft = 128;
spectrogram(sig,windowlength,noverlap,nfft,sFMCW.SampleRate,'yaxis')
I = real(sig);
Q = imag(sig);
save('fmcw1.mat','I','Q');
```

List of References

[1] R. Wiley, *The interception and analysis of radar signals*, 2nd ed. Norwood, MA: Artech House, 2006, pp. 1–8.

[2] K. Igarashi and K. Kikuchi, "Optical signal processing by phase modulation and subsequent spectral filtering aiming at applications to ultrafast optical communication systems," *IEEE Journal of Selected Topics in Quantum Electronics*, vol. 14, no. 3, pp. 551–565, May 2008.

[3] M. R. Arvizo, J. Calusdian, K. B. Hollinger, and P. E. Pace, "Robust symmetrical number system preprocessing for minimizing encoding errors in photonic analog-to-digital converters," *Optical Engineering*, vol. 50, no. 8, 2011.

[4] G. L. Fudge, R. E. Bland, M. A. Chivers, S. Ravindran, J. Haupt, and P. E. Pace, "A nyquist folding analog-to-information receiver," in *42nd Asilomar Conference on Signals, Systems and Computers*, Oct 2008, pp. 541–545.

[5] R. Maleh, G. L. Fudge, F. A. Boyle, and P. E. Pace, "Analog-to-information and the nyquist folding receiver," *IEEE Journal on Emerging and Selected Topics in Circuits and Systems*, vol. 2, no. 3, pp. 564–578, Sept 2012.

[6] P. E. Pace, A. Kusmanoff, and G. L. Fudge, "Nyquist folding analog-to-information receiver: Autonomous information recovery using quadrature mirror filtering," in *Conference Record of the Forty-Third Asilomar Conference on Signals, Systems and Computers*, Nov 2009, pp. 1581–1585.

[7] A. Yariv and P. Yeh, *Photonics: Optical Electronics in Modern Communications*, 6th ed. Madison Avenue, NY: Oxford University Press, 2007, pp. 694–697.

[8] A. Yariv and P. Yeh, *Photonics: Optical Electronics in Modern Communications*, 6th ed. New York, NY: Oxford University Press, 2007, p. 426.

[9] T. W. Tedesso, "Use of symmetrical number systems in electronic warfare," Ph.D. dissertation, Dept. Elect. and Comp. Eng., Naval Postgraduate School, Monterey, CA, 2013.

[10] Y. Li, Y. Zhang, and Y. Huang, "Slope value detection-based ditherless bias control technique for Mach–Zehnder modulator," *Optical Engineering*, vol. 52, no. 8, pp. 87–109, 2013.

[11] A. Yariv and P. Yeh, *Photonics: Optical Electronics in Modern Communications*, 6th ed. New York, NY: Oxford University Press, 2007, pp. 521–523.

[12] P. E. Pace, *Detecting and Classifying Low Probability of Intercept Radar*, 2nd ed. Norwood, MA: Artech House, 2009, pp. 86–94.

[13] T. Okamoto and F. Ito, "Ultrafast linear optical sampling technique for optical communication systems," in *Opto-Electronics and Communications Conference*, June 2015, pp. 1–3.

[14] P. E. Pace, *Advanced Techniques for Digital Receivers*, 1st ed. Norwood, MA: Artech House, 2000, pp. 84–85.

[15] R. Shmel and P. E. Pace, "Photonic compressed sensing nyquist folding receiver," in *IEEE International Photonics Conference*, Oct 2017.

[16] M. Nixon and A. Aguado, *Feature Extraction and Image Processing*, 1st ed. Jordon Hill, Oxford: Newnes, 2004, pp. 76–79.

Initial Distribution List

1. Defense Technical Information Center
   Ft. Belvoir, Virginia

2. Dudley Knox Library
   Naval Postgraduate School
   Monterey, California